Tumor Protein D54 is a promiscuous Rab effector

Gabrielle Larocque[1], **Penelope J. La-Borde**[1], **Nicholas I. Clarke**[1], **Stephen J. Royle**[1]

***For correspondence:** s.j.royle@warwick.ac.uk (SJR)

[1]Centre for Mechanochemical Cell Biology, Warwick Medical School, Gibbet Hill Road, Coventry, CV4 7AL, UK

Abstract Intracellular membrane traffic is coordinated by Rab GTPases and their effector proteins. Here, we investigated the function in human cells of Tumor Protein D54 (TPD54/TPD52L2), a member of the TPD52-like protein family. Our initial experiments suggested that TPD54 has a role in anterograde membrane traffic and in the recycling of endocytosed proteins back to the cell surface. To understand how TPD54 controls these diverse functions, we used an inducible method to reroute TPD54 to mitochondria. Surprisingly, this manipulation resulted in the capture of many functional vesicles (30 nm diameter) at the mitochondrial surface. To investigate the identity of captured vesicles, we did a rerouting screen using TPD54 as bait and the Rab GTPases as prey. This screen revealed that TPD54 associates promiscuously with at least 16 out of 43 different Rab GTPases. Our data suggest that TPD54 binds as an effector protein to Rabs involved in anterograde traffic and recycling.

Introduction

Eukaryotic cells are by definition compartmentalized: they contain organelles and membrane-bound domains that have distinct identities. Vesicle transport between these locations is tightly regulated to maintain these identities yet allow exchange of specific materials. The Rab subfamily of small GTPases and their effector proteins are central to the control and regulation of vesicle transport. Rabs exist in two different nucleotide-bound conformations. A GDP-bound Rab is inactive and associates with a GDP-dissociation inhibitor (GDI) so that it may be extracted and transported to the appropriate donor membrane where it is stabilized by a guanine nucleotide exchange factor (GEF) (***Wu et al., 2010***; ***Pylypenko et al., 2006***; ***Blümer et al., 2013***). The GEF activates the Rab, exchanging GDP for GTP, and the active GTP-bound Rab can now recruit an effector protein (***Müller and Goody, 2018***). The roles of Rab effector proteins range from the formation of the vesicle, to its transport or its subsequent fusion (***Johansson et al., 2007***; ***Semerdjieva et al., 2008***; ***Murray et al., 2016***). When the vesicle reaches the acceptor membrane, a GTPase-activating protein (GAP) inactivates the Rab and a GDI extracts the Rab for the cycle to begin again (***Müller and Goody, 2018***). There are more than 60 Rab proteins in humans, each having a definite set of interactors: GEFs, GAPs and effectors (***Barr and Lambright, 2010***; ***Pylypenko et al., 2018***). Identifying Rab interactors to understand how Rab GTPases orchestrate membrane traffic is a major goal in cell biology (***Kanno et al., 2010***; ***Koch et al., 2016***; ***Gillingham et al., 2014***).

In humans, there are four Tumor Protein D52-like proteins (TPD52-like proteins: TPD52, TPD53/TPD52L1, TPD54/TPD52L2 and TPD55/TPD52L3) some of which have been associated with membrane trafficking but the cell biological roles of the family are not well characterized. TPD52-like proteins are short (140 to 224 residues), have 50 % identity and each contain a coiled-coil domain through which they can homo- and heterodimerize. All are ubiquitously expressed with the exception of TPD55, which is restricted to testis (***Cao et al., 2006***). TPD52 was the first of the family

to be identified due to its overexpression in cancer, and it is still the best studied. However, all members have been found to be overexpressed in a series of cancers (***Cao et al., 2006***; ***Byrne et al., 1995***, ***1998***; ***Nourse et al., 1998***). Overexpression of TPD52 correlates with poor prognosis in breast cancer patients and in cell models, TPD52 overexpression promotes proliferation and invasion (***Byrne et al., 2010***, ***1996***; ***Li et al., 2017***; ***Dasari et al., 2017***).

Rather disparate membrane trafficking functions have been reported for TPD52 and TPD53. First, TPD52 is involved in secretion in pancreatic acinar cells (***Thomas et al., 2004***, ***2010***; ***Messenger et al., 2013***). Second, membrane trafficking proteins bind to TPD52, such as the endocytic protein Rab5c (***Shahheydari et al., 2014***), and the transcytotic protein MAL2 (***Wilson et al., 2001***). Third, TPD52 has a role in lipid droplet biogenesis at the Golgi (***Kamili et al., 2015***) Finally, a role in membrane fusion was proposed for TPD53 (***Proux-Gillardeaux et al., 2003***). By contrast, the potential functions of TPD54 remain unexplored.

What is striking about TPD54 is its sheer abundance in cells. Previous quantitative proteomic analyses revealed that TPD54 is one of the most abundant proteins in HeLa cells, ranked 180th out of 8,804 (***Hein et al., 2015***; ***Kulak et al., 2014***). There are an estimated 3.3×10^6 copies of TPD54 per HeLa cell (2.7 µM), whereas abundant membrane traffic proteins such as clathrin light chain A or β2 subunit of AP2 total 2.2×10^6 or 1.0×10^5 copies (1.8 µM or 0.4 µM), respectively (***Hein et al., 2015***). Despite its abundance, there are virtually no published data on the cell biology of TPD54. Due to sequence similarity and heterodimerization properties, we hypothesized that TPD54, like the other members of the family, would also be involved in membrane trafficking. We set out to investigate the cell biology of TPD54 and found that it is associated with small transport vesicles where it acts as an effector to at least one-quarter of the Rab GTPase family. Our experiments highlight roles for TPD54 in regulating anterograde membrane traffic as well as recycling of internalized receptors.

Results

TPD54 is a membrane trafficking protein

To investigate the subcellular localization of TPD54, we tried to make antibodies to see TPD54 by immunofluorescence microscopy. We did not succeed and therefore we generated a cell line where TPD54 was endogenously tagged with monomeric GFP (***Figure 1–Figure Supplement 1***). GFP-TPD54 fluorescence was diffuse in the cytoplasm, but was also seen at the Golgi apparatus, marked with GalT-mCherry, and on endosomes, marked by APPL1 and OCRL1. It also colocalized with various membrane trafficking proteins, such as clathrin light chain a and the R-SNARE, VAMP2 ***Figure 1***A. A similar pattern was seen by overexpression of mCherry-tagged TPD54 in parental cells (***Figure 1–Figure Supplement 2***). These observations suggest that TPD54 is a protein associated with membrane trafficking.

As a next step to characterizing TPD54, we investigated the binding partners of TPD54. To do so, we performed an immunoprecipitation (IP) of GFP-tagged TPD54 from HeLa cell lysates and analyzed co-precipitating proteins by mass spectrometry ***Figure 1***B. We found that two other members of the TPD52-like family, TPD52 and TPD53, were significantly enriched in the TPD54 samples versus control. TPD52, TPD53 and TPD54 have been reported to heterodimerize (***Byrne et al., 1998***), and this suggested that our assay was able to detect binding partners of TPD54. Among the other significant hits, we found the Rab GTPases Rab14, Rab2a and Rab5c. Rab14 has been identified as a regulator of the transport between the Golgi apparatus and early endosomes (***Junutula et al., 2004***), as well as from the Golgi apparatus to the plasma membrane (***Kitt et al., 2008***). Rab2a is on the endoplasmic reticulum (ER) to Golgi pathway (***Tisdale et al., 1992***), and Rab5c is found on the endocytic pathway (***Bucci et al., 1995***). Taken together, the results confirm that TPD54 is a protein involved in membrane trafficking.

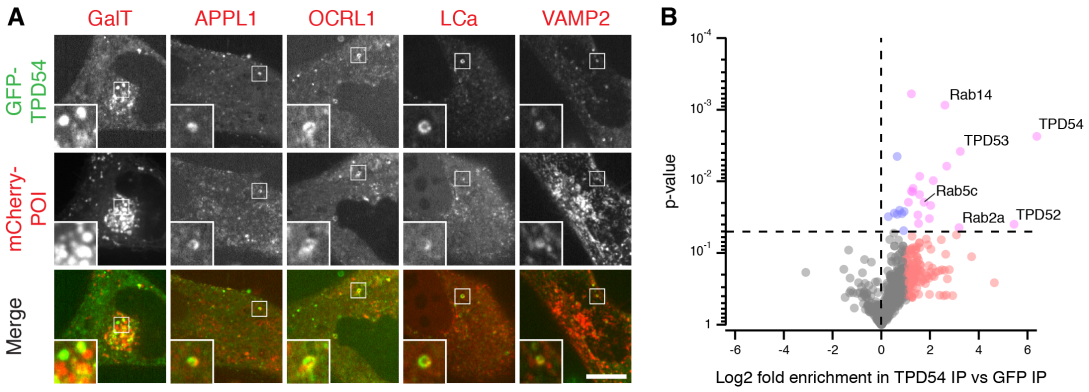

Figure 1. TPD54 is a membrane trafficking protein.
(**A**) Representative confocal micrographs showing the colocalization of transiently expressed mCherry-tagged membrane trafficking proteins with endogenously tagged GFP-TPD54. Inset: 3X zoom. Scale bar, 10 µm. (**B**) Volcano plot of a comparative mass spectrometry analysis of GFP-TPD54 vs GFP co-immunoprecipitation. Proteins enriched more than two-fold in GFP-TPD54 samples compared to GFP are shown in red or pink. Those $p < 0.05$ are shown in blue or pink, $n = 4$. Note, glycogen debranching enzyme (3.7-fold increase, $p = 1.09 \times 10^{-8}$) is not shown. Proteomic data and volcano plot calculations (***Figure 1–source data 1*** and ***Figure 1–source data 2***).

Figure 1–Figure supplement 1. HeLa cell line with endogenously GFP-tagged TPD54

Figure 1–Figure supplement 2. Overexpressed TPD54 colocalizes with membrane trafficking components.

Figure 1–source data 1. Proteomic data set.

Figure 1–source data 2. Volcano plot data.

TPD54 regulates the anterograde and recycling pathways

To investigate potential functions of TPD54, we sought to identify trafficking defects caused by the loss of TPD54. Using RNAi to deplete TPD54 in HeLa cells, we first assessed the transport of cargoes from the ER to the Golgi apparatus, and from the Golgi to the plasma membrane (PM) with the RUSH (retention using selective hooks) system (***Boncompain et al., 2012***). Briefly, the RUSH system allows the synchronous release of a reporter (here, GFP-tagged E-cadherin with a streptavidin-binding domain) from an ER-localized hook (here, streptavidin fused to a KDEL motif) by addition of biotin. After release, EGFP-E-cadherin is transported from the ER to the PM, via the Golgi apparatus. In control cells, the reporter reached maximal intensity at the Golgi between 14 and 28 minutes after release and then left the Golgi for the PM (***Figure 2***A and ***Figure 2–video 1***). By contrast, TPD54-depleted cells had obviously delayed kinetics (***Figure 2–video 2***). We quantified the fluorescence of the reporter at the Golgi and expressed it as a fraction of the total cell fluorescence (***Figure 2***B). The resulting data were best described by a logistic function representing ER-to-Golgi transport and a line fit to describe Golgi-to-PM (***Figure 2***C-D, see Methods). This automated procedure allowed us to find the half-time ($T_{1/2}$) for ER-to-Golgi and ER-to-PM transport, and also infer the Golgi transport time as the difference between these times (***Figure 2***E-G). The data suggest that TPD54-depleted cells have delayed export of E-Cadherin at all stages.

We also wanted to know if TPD54 was required for endocytosis or cargo recycling, since Rab5c was one of our mass spectrometry hits (***Figure 1***B). To do so, we performed a transferrin uptake and recycling assay in TPD54-depleted and control HeLa cells. The internalization of transferrin was unchanged, but recycling to the plasma membrane was slower in TPD54-depleted cells (***Figure 2***H). In these experiments, the efficiency of the depletion was checked by western blot analysis, using α-tubulin as a loading control (***Figure 2***I). These results suggest that TPD54 operates in several steps of the anterograde pathway and in endosomal recycling.

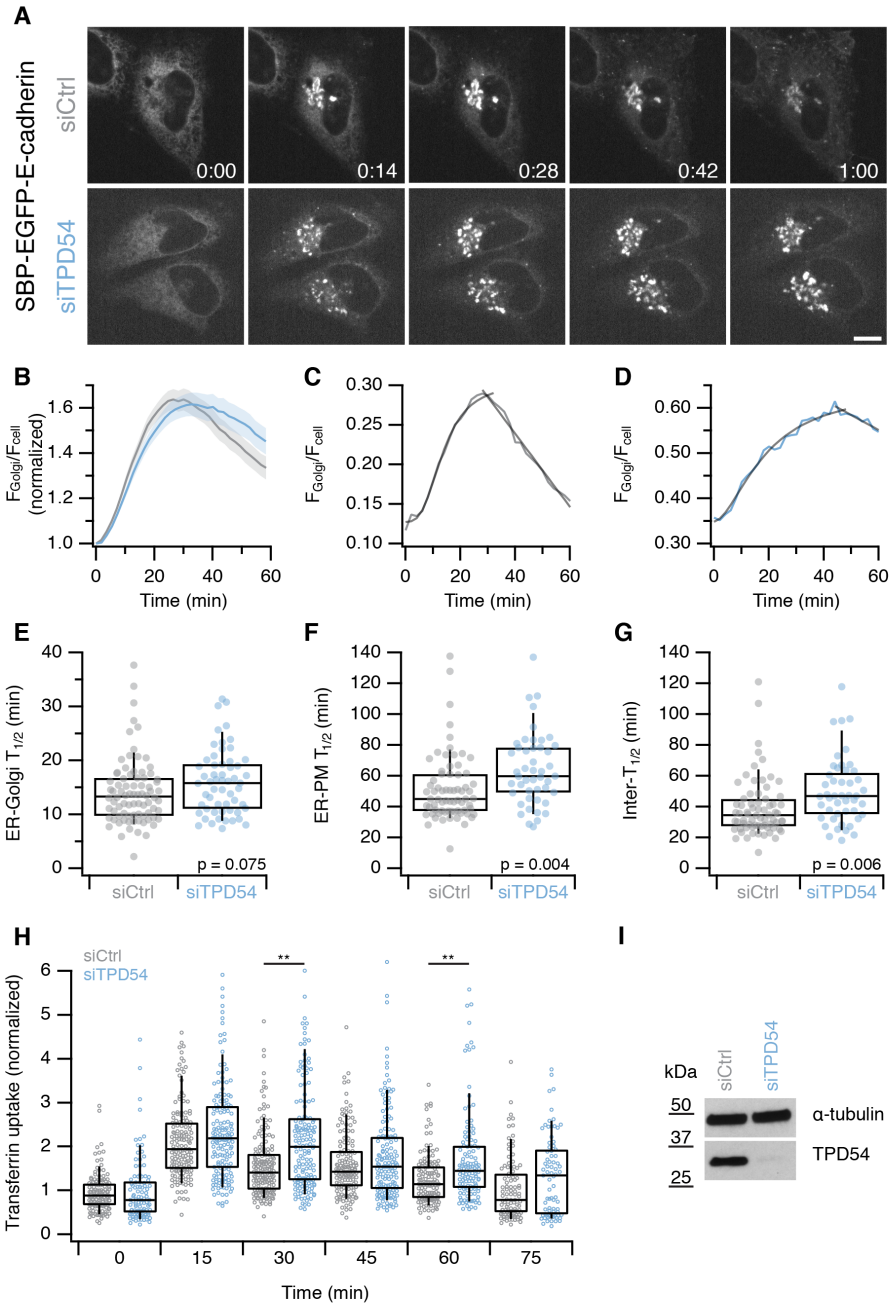

Figure 2. TPD54-depleted cells have defective anterograde membrane traffic and cargo recycling.
(**A**) Still confocal images of RUSH experiments. SBP-EGFP-E-cadherin localization in control (siCtrl) and TPD54-depleted (siTPD54) HeLa cells at the indicated times (min) after biotin treatment. Scale bar, 10 µm. (**B**) Normalized fraction of total E-cadherin fluorescence at the Golgi as a function of time, in control (gray) or TPD54-depleted (blue) cells. Line and shaded area, mean ± s.e.m. (**C-D**) Single cell traces of the E-cadherin fluorescence ratio of a control (gray) or TPD54-depleted (blue) cell, fitted with a logistic function and a line. (**E-G**) Box plots showing the half-times of E-cadherin transport from ER-to-Golgi (E) and from ER-to-PM (G) in control and TPD54-depleted cells. The difference in half-times represents intra-Golgi transport (F). P values from Student's t-test with Welch's correction. (**H**) Box plot showing the uptake and recycling of transferrin in control and TPD54-depleted cells. For all box plots, boxes show IQR, bar represents the median and whiskers show 9th and 91st percentile. Wilcoxon Rank Test, **, $p < 0.01$ (**I**) Western blot to assess the depletion of TPD54 by RNAi. The protein level of TPD54 and α-tubulin (loading control) is shown.

Figure 2–video 1. SBP-EGFP-E-Cadherin RUSH imaging in control cells. Time, hh:mm. Scale bar, 10 µm.

Figure 2–video 2. SBP-EGFP-E-Cadherin RUSH imaging in TPD54-depleted cells. Time, hh:mm. Scale bar, 10 µm.

Rerouting TPD54 to mitochondria allows detection of its associated proteins

To better understand the pathways on which TPD54 functions, we wanted to test which proteins co-reroute with TPD54 when it is rerouted to mitochondria using rapamycin-induced heterodimerization. Proteins tagged with an FK506-binding protein (FKBP) domain can be rerouted to MitoTrap, a mitochondrially-targeted FRB domain, by the addition of rapamycin (***Robinson et al., 2010***). As expected, mCherry-FKBP-TPD54 but not mCherry-TPD54 was efficiently rerouted to mitochondria with this method (***Figure 3***A). The kinetics of rerouting was reasonably fast, with TPD54 appearing at mitochondria 6 s post-rapamycin (***Figure 3***B-C, ***Figure 3–video 1***). The increase in mitochondrial TPD54 was best fit by a single exponential function (χ^2 = 0.43, τ = 37.98 $\pm$ 0.38 s) while the loss in cytoplasmic signal followed similar kinetics (τ = 47.52 $\pm$ 0.21 s, ***Figure 3***B). Although the kinetic analysis suggested a single process, close inspection of the movies suggested that the pool of TPD54 which is apparently cytosolic is rerouted first, making visible a small number of endosomes (***Figure 3***C, arrow), before they also became rerouted leaving no detectable TPD54 away from the mitochondria (***Figure 3***E, 4 min).

To test if TPD54-binding proteins become co-rerouted to the mitochondria in this assay (***Figure 3***D), we used TPD52. TPD52 is a TPD52-like protein family member that can heterodimerize with TPD54 (***Byrne et al., 1998***) and was also detected in our mass spectrometry analysis (***Figure 1***B). As shown in ***Figure 3***E, TPD52 is efficiently co-rerouted with TPD54, suggesting that the rerouting method can be used as a way to find proteins that associate with TPD54. During our TPD54 rerouting experiments we noticed that once the rerouting was complete, mitochondrial morphology changed and that mitochondria began to aggregate (***Figure 3***C).

Mitochondrial rerouting of TPD54 results in vesicle capture

To investigate why mitochondrial morphology became altered at later time-points after rerouting TPD54, we used electron microscopy (EM) to examine the ultrastructure of mitochondria at different time-points (***Figure 4***). Cells expressing MitoTrap and mCherry-FKBP-TPD54 were imaged as rapamycin was applied (***Figure 4***A). They were then fixed at various times after rerouting and the same cells were then imaged by EM. The mitochondrial TPD54 signal was partial 20 s post-rapamycin, after 5 min the signal was maximal, and after 30 min, mitochondrial aggregation was observed by light microscopy ***Figure 4***A-B. At the EM level, in cells where TPD54 was rerouted, mitochondria were decorated with numerous small vesicles. After 5 min or 30 min, it was clear that mitochondria had become aggregated because the vesicles had contacted more than one mitochondrial surface. We segmented the mitochondrial and vesicular profiles to analyze this effect in more detail (***Figure 4***C). The vesicles captured after TPD54 rerouting are small, homogeneous (29.9 $\pm$ 9.4 nm) and do not change size over time (***Figure 4***D-E). The number of vesicles captured per unit length of mitochondrial perimeter increases with time and the perimeter lengths that remain undecorated decreases (***Figure 4***E). We noted significant vesicle capture at the earliest time-point we could study, 20 s post-rapamycin. Mitochondria in control cells are essentially undecorated with the occasional vesicle coinciding with our detection criteria, confirming that vesicle capture is a result of TPD54 rerouting to mitochondria. These experiments explain the mitochondrial aggregation but also change our interpretation of the rerouting experiments. Any proteins which co-reroute with TPD54 may be binding directly to TPD54, but they may also be simply resident on the same vesicle.

TPD54 localizes to a small number of large puncta in cells with the remainder being cytoplasmic (***Figure 1***A). Could it be that the cytoplasmic localization of TPD54 actually corresponds to a large population of TPD54-positive vesicles that were below the resolution limit of the microscope? Close inspection of live cell imaging data showed that the cytoplasmic TPD54 signal flickered, whereas free GFP did not ***Figure 5–video 1***, suggesting that the cytoplasmic GFP-TPD54 signal is mainly vesicular. To address this point quantitatively, we used fluorescence recovery after photobleaching (FRAP) to assess diffusion and/or exchange of GFP-TPD54 at sub-resolution structures (summarized in ***Figure 5*** and ***Table 1***). FRAP kinetics were much slower for GFP-TPD54 (either expressed or endogenous) compared to GFP, suggesting diffusion-coupled binding of GFP-TPD54 to membranes.

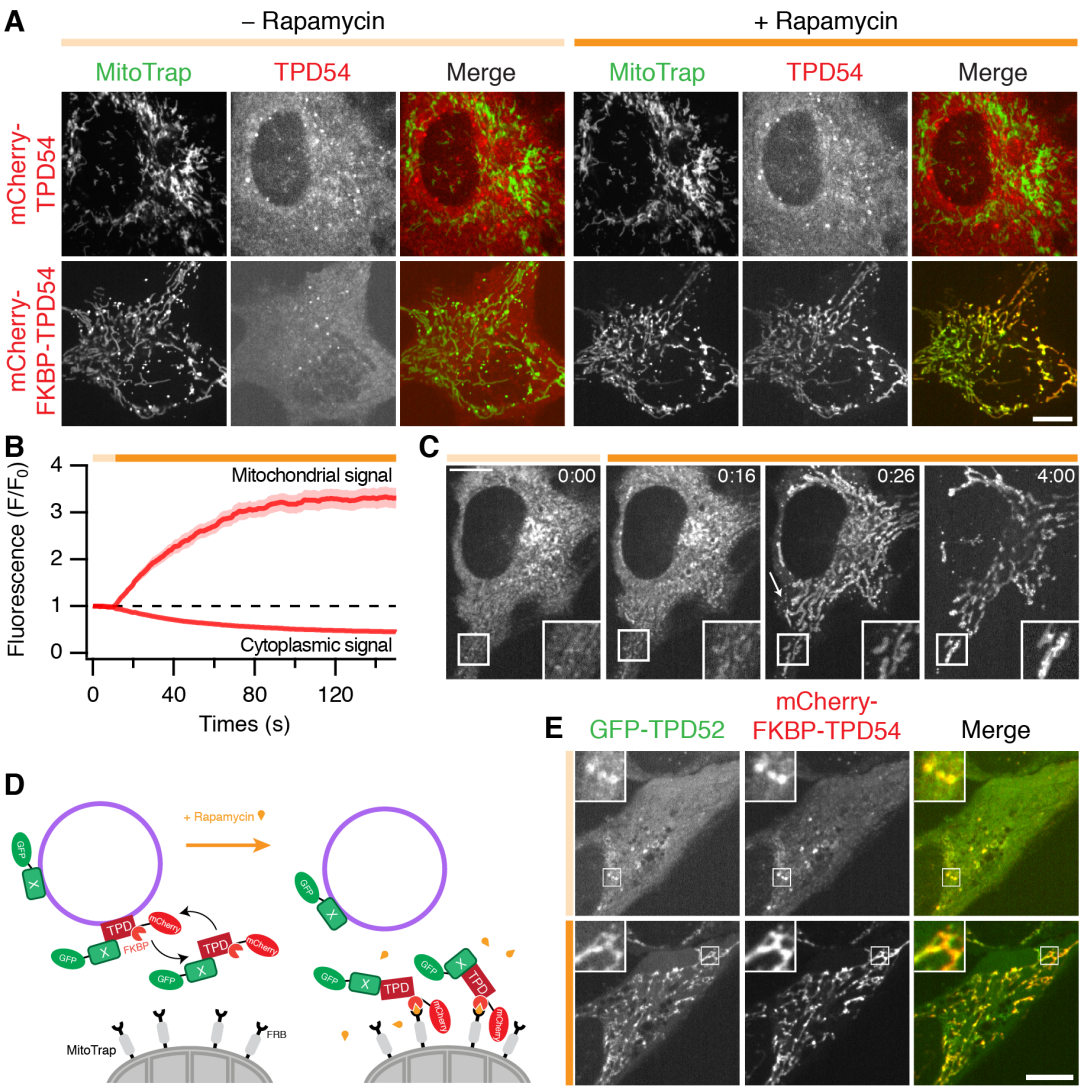

Figure 3. TPD54 can be rerouted efficiently to mitochondria and associated proteins become co-rerouted.

(**A**) Confocal micrographs showing the rerouting of mCherry-FKBP-TPD54 but not mCherry-TPD54 to mitochondria in cells co-expressing YFP-MitoTrap, after addition of 200 nM rapamycin (orange bar). (**B**) Kinetics of mCherry-FKBP-TPD54 rerouting. The mitochondrial and cytoplasmic signal of mCherry-FKBP-TPD54 as a function of time after the addition of 200 nM rapamycin at 10 s. Line and shaded area show the mean ± s.e.m., $n = 16$. (**C**) Still images from a TPD54 rerouting movie. Arrow: endosomes become visible after removal of the cytoplasmic pool of TPD54. Time, mm:ss (Rapamycin at 00:10). Scale bars, 10 µm. Insets, 2× zoom. (**D**) Schematic diagram to show how rerouting of TPD54 to mitochondria can be used to identify binding partners by co-rerouting. (**E**) Confocal micrographs showing the co-rerouting of GFP-TPD52 with mCherry-FKBP-TPD54 to mitochondria.

Figure 3–video 1. Rerouting mCherry-FKBP-TPD54 to mitochondria in cells co-expressing MitoTrap. Time, mm:ss. Scale bar, 10 µm

.

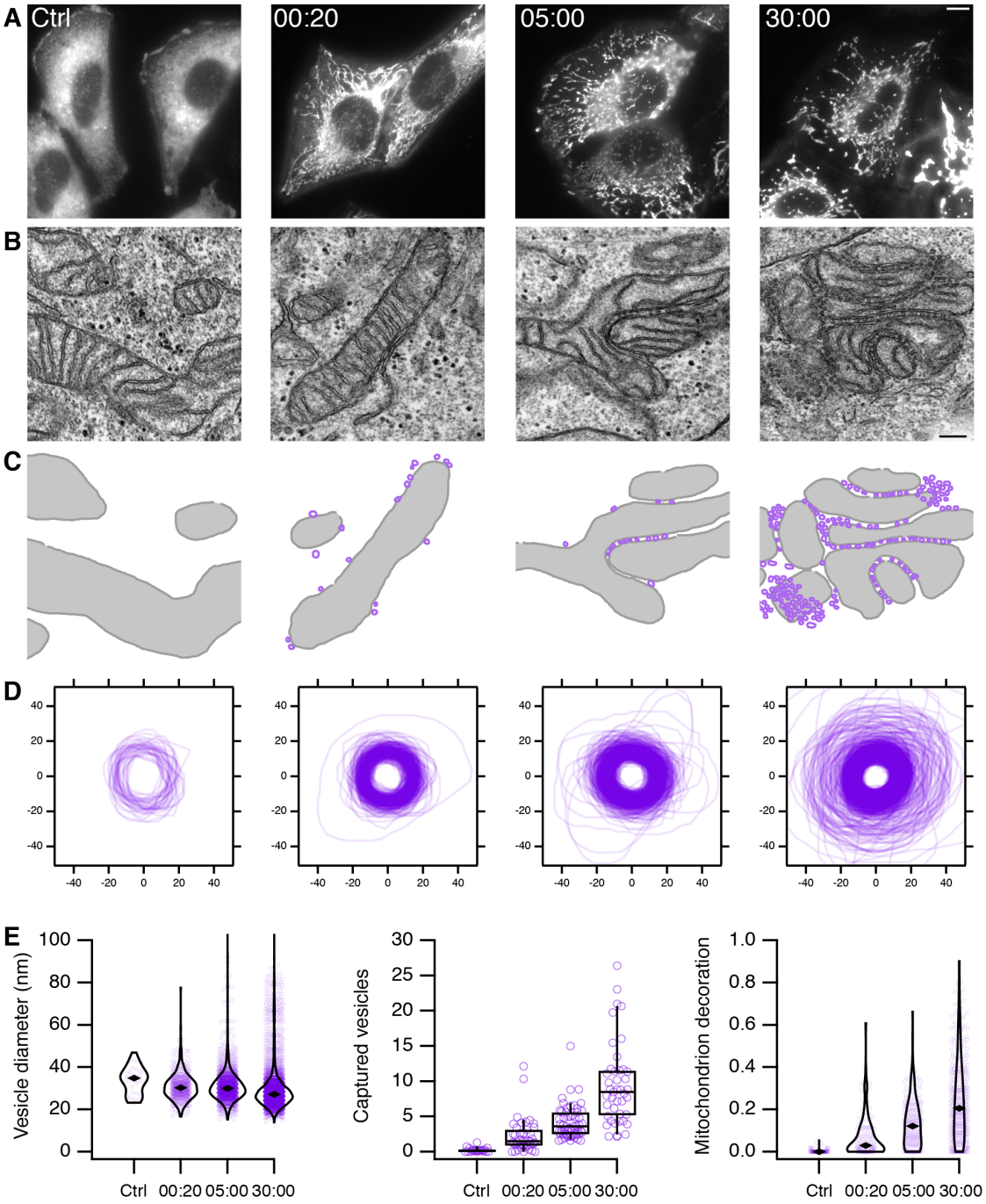

Figure 4. Capture of small vesicles by rerouting TPD54 to mitochondria.
(**A**) Fluorescence microscopy images of mCherry-FKBP-TPD54 in HeLa cells. Cells expressing mCherry-FKBP-TPD54 and dark MitoTrap were fixed after no rapamycin application (Ctrl) or after 20 s, 5 min or 30 min of rapamycin addition (200 nM). The pictured cell was then imaged by electron microscopy. Scale bar, 10 µm. (**B**) Sample electron micrographs of the cells shown in A. Scale bar, 200 nm. (**C**) Segmented view of mitochondria (gray) and vesicles (purple) in the images shown in B. (**D**) Profiles of segmented vesicles from electron micrographs. All vesicles segmented from the control dataset are shown with a random sample from the treatment groups as a comparison. The sample size is in proportion to the capture of vesicles at the mitochondria (34, 320, 594, 1347 for ctrl, 20 s, 5 min and 30 min respectively). (**E**) Violin plot to show the diameter of vesicles imaged in each dataset. Spots represent individual vesicles. Marker shows the median. Box plot to show the number of vesicles captured per 1 µm of mitochondrial membrane. Spots show the number per micrograph in each dataset. Box shows the IQR, median and whiskers show 9th and 91st percentiles. Violin plot to show the fraction of mitochondrial membrane that is decorated with vesicles. Spots show individual mitochondria from the dataset. See Methods for details.

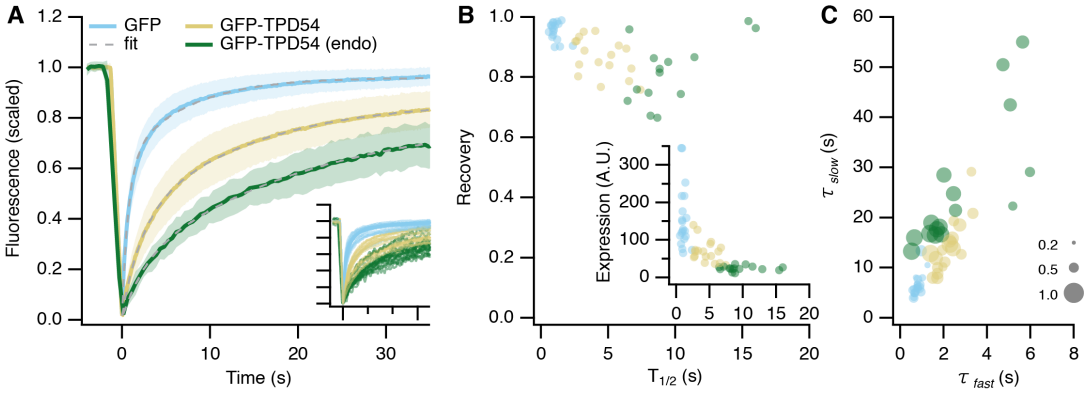

Figure 5. Fluorescence recovery after photobleaching (FRAP) analysis of GFP-TPD54.
(**A**) FRAP data for GFP-TPD54 in knock-in cells (endo), expressed GFP or GFP-TPD54 in parental cells. Lines and shaded areas show mean ± 1 s.d. Dotted line shows a double exponential function fitted to the average data. The fit co-efficients are summarized in ***Table 1***. Inset: FRAP data from different cells colored as indicated and displayed on the same axes range. (**B**) Recovery (mobile fraction) of individual fits to FRAP data plotted against $T_{1/2}$. Inset: Initial cellular fluorescence as a function of $T_{1/2}$. (**C**) Plot to show FRAP kinetics in individual cells. τ_{slow} is plotted against τ_{fast} and marker size indicates the fraction recovered by the slow process. Markers represent individual cells and colors indicate the protein being imaged.

Figure 5–video 1. Fluorescence recovery after photobleaching (FRAP) of GFP (left) or GFP-TPD54 (right) expressed in HeLa cells. Bleach area is a rectangle inset by 0.8 µm. Scale bar, 5 µm. (endogenous).

Table 1. Kinetics of fluorescence recovery after photobleaching (FRAP).

Protein	Recovery	τ_{fast} (s)	τ_{slow} (s)	Fast (%)	Slow (%)
GFP	0.960	0.74	6.90	62.4	37.6
GFP-TPD54	0.868	2.14	13.40	40.9	60.1
GFP-TPD54 (endogenous)	0.703	2.41	20.25	23.1	76.9

There were two phases of GFP-TPD54 recovery, a small fast process (τ = 2 s) with the majority of recovery via a slow process, which was on the order of tens of seconds. These kinetics were consistent with the majority of TPD54 binding to subcellular structures, with a minor fraction being cytosolic. Analysis of individual FRAP traces showed that in cells expressing higher levels of GFP-TPD54, FRAP was faster and that this was due to a larger fraction recovering via the fast process (***Figure 5***B). These experiments indicate that the freely diffusing pool of TPD54 is minimal and the majority of TPD54 is associated with small vesicles below the resolution limit. This conclusion is consistent with the vesicle capture by mitochondria during TPD54 rerouting.

Vesicles captured by TPD54 rerouting to mitochondria are functional

The small size of the vesicles captured by TPD54 rerouting to mitochondria raised the question of whether or not they were functional. As a first step to answering this question, we sought to identify the vesicles' cargo. To do this, we tested five model cargoes where the alpha chain of CD8 is fused to different peptides that bear various endocytic motifs (***Kozik et al., 2010***). Briefly, CD8-FANPAY, CD8-YAAL or CD8-EAAALL have a single YXXϕ, [F/Y]XNPX[Y/F] or [D/E]XXXL[L/I/M] motif, respectively. CD8-CIMPR has the tail of the cation-independent mannose-6-phosphate receptor (CIMPR), which contains at least four endocytic motifs including two of the dileucine type. As a control, CD8-8xA was used which has eight alanines, no endocytic motif and cannot be internalized. We examined the subcellular distribution of these cargoes in cells where TPD54 had been rerouted to mitochondria. In the control condition with no addition of rapamycin, all CD8 constructs were in endosomes or in the case of CD8-8xA, at the plasma membrane. After rerouting, the localization

of CD8-8xA, CD8-FANPAY and CD8-YAAL was unaffected, whereas CD8-EAAALL and CD8-CIMPR were co-rerouted with TPD54 to the mitochondria (***Figure 6***A). To ensure that this co-rerouting was genuine and not a peculiarity of the model cargoes, we confirmed that endogenous CIMPR also co-rerouted with TPD54 (***Figure 6***B). This suggested that vesicles with cargo harbouring a dileucine motif were preferentially captured by TPD54 rerouting (***Figure 6***C).

Receptors containing dileucine endocytic motifs are internalized at the PM and then recycled either via recycling endosomes or the Golgi apparatus. We therefore labeled CD8-EAAALL at the surface with Alexa 488-conjugated anti-CD8 antibodies, allowed internalization and trafficking to proceed, and at different time-points, performed mitochondrial vesicle capture via TPD54 rerouting (***Figure 6***D). Capture of surface-labeled CD8-EAAALL occurred at time-points greater than 60 min after internalization (***Figure 6***E). These experiments indicate that dileucine motif-containing receptors transit via the vesicles which can be captured on mitochondria by TPD54 rerouting, but only at late time points after internalization. The time course of capture is consistent with recycling of endocytic cargo from the Golgi apparatus.

A second test of vesicle functionality is whether the vesicles contain the machinery for fusion. Accordingly, we tested for co-rerouting of endogenous SNAREs in our vesicle capture assay. Generally, vesicle-resident R-SNAREs but not target membrane-resident Q-SNAREs were co-rerouted with TPD54 to mitochondria. We found co-rerouting of the R-SNAREs VAMP2, VAMP3, VAMP7 and VAMP8, but not the Q-SNAREs STX6, STX7, STX8, STX10 or STX16 (***Figure 7***). There was some evidence of selectivity with the localization of the R-SNARE VAMP4 being unaffected by TPD54 rerouting. Together these experiments indicate that, despite their small size, the vesicles captured by TPD54 rerouting are functional: they contain specific cargo and they have R-SNAREs for fusion. Moreover the presence of different SNAREs, suggests that although the captured vesicles appear morphologically homogeneous, they are likely to be a crowd of different vesicle identities.

TPD54 is associated with multiple Rab GTPases

What are the identities of the vesicles captured by TPD54 rerouting? To answer this question, we screened 43 GFP-tagged Rab GTPases for co-rerouting with mCherry-FKBP-TPD54 to dark MitoTrap. The collection of GFP-Rabs tested covers a range of membrane trafficking pathways (***Yoshimura et al., 2007***; ***Zhen and Stenmark, 2015***; ***Wandinger-Ness and Zerial, 2014***). The results of the screen are presented in ***Figure 8***, with examples of positive and negative hits shown in ***Figure 8–Figure Supplement 1***.

Significant co-rerouting was detected for 16 out of 43 Rabs. These positive hits were: Rab30, Rab25, Rab26, Rab45, Rab14, Rab11a, Rab12, Rab1a, Rab43, Rab1b, Rab10, Rab33b, Rab19, Rab33a, Rab37 and Rab2a (listed by descending effect size, ***Figure 8***C). Some evidence for co-rerouting of Rab38, Rab5c and Rab35 was seen, although in any individual trial no clear difference was observed. The localization of the other 24 Rabs was unaffected by rerouting of TPD54 and was indistinguishable from GFP. Rab30 was the most efficiently co-rerouted Rab, with the post-rerouting signal being 2.5 fold higher than before TPD54 rerouting (***Figure 8–video 1***). The smallest effect that we could reliably detect was Rab2a, with a 1.4 fold increase.

If the relocalization of Rabs observed in the screen was the result of co-rerouting with TPD54, a correlation between the extent of rerouting for a Rab and TPD54 is predicted (***Figure 8***D). This was broadly true, with a positive correlation observed for almost all of our positive hits, and a low, flat relationship for negative Rabs. Rab14 was an exception. Here the relationship was high and flat indicating that Rab14 rerouting was maximal even after modest TPD54 rerouting.

We next performed a test of reciprocality, by asking if mCherry-TPD54 was co-rerouted to mitochondria when a GFP-FKBP-Rab was rerouted to dark MitoTrap using 200 nM rapamycin. We tested two positive hits from our screen, Rab11a and Rab25 as well as Rab7a, a negative Rab (***Figure 8–Figure Supplement 2***). Rerouting of either Rab11a or Rab25 caused co-rerouting of TPD54, while rerouting Rab7a to mitochondria had no effect on TPD54 localization. Interestingly, we noticed that when Rab11a or Rab25 were rerouted, there was still a number of TPD54-positive structures,

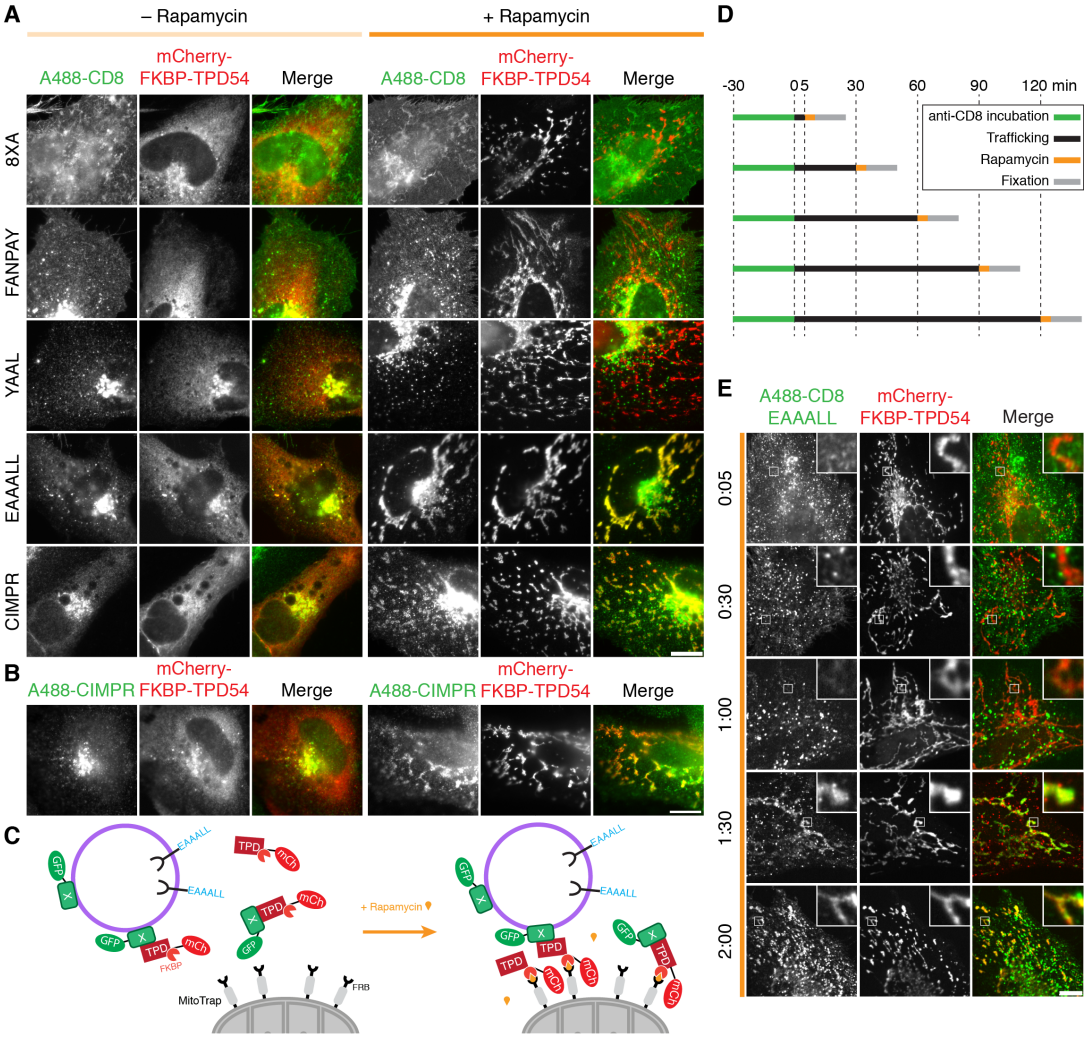

Figure 6. TPD54 co-reroutes dileucine motif-containing receptors only.
(**A**) Representative widefield micrographs of cells co-expressing mCherry-FKBP-TPD54, dark MitoTrap and the indicated CD8 construct. Rerouting was induced by 200 nM rapamycin. Cells were fixed, permeabilized and stained for total CD8. (**B**) Representative widefield micrographs showing co-rerouting of endogenous CIMPR detected by immunofluorescence with rerouting of mCherry-FKBP-TPD54 to dark MitoTrap by addition of 200 nM rapamycin. (**C**) Diagram of the revised interpretation of TPD54 rerouting experiments. When TPD54 is rerouted to the mitochondria, it reroutes the small vesicles with which it is associated. These vesicles contain cargo with a dileucine motif. (**D**) Pulse label and timed vesicle capture experiments. Cells expressing CD8-EAAALL were surface labeled with Alexa488-conjugated anti-CD8 antibodies for 30 min, then incubated at 37 °C for the indicated time (min), treated with 200 nM rapamycin for 5 min and fixed. (**E**) Representative widefield micrographs from a pulse label and timed vesicle capture experiment. Inset, 5× zoom. Scale bars, 10 µm.

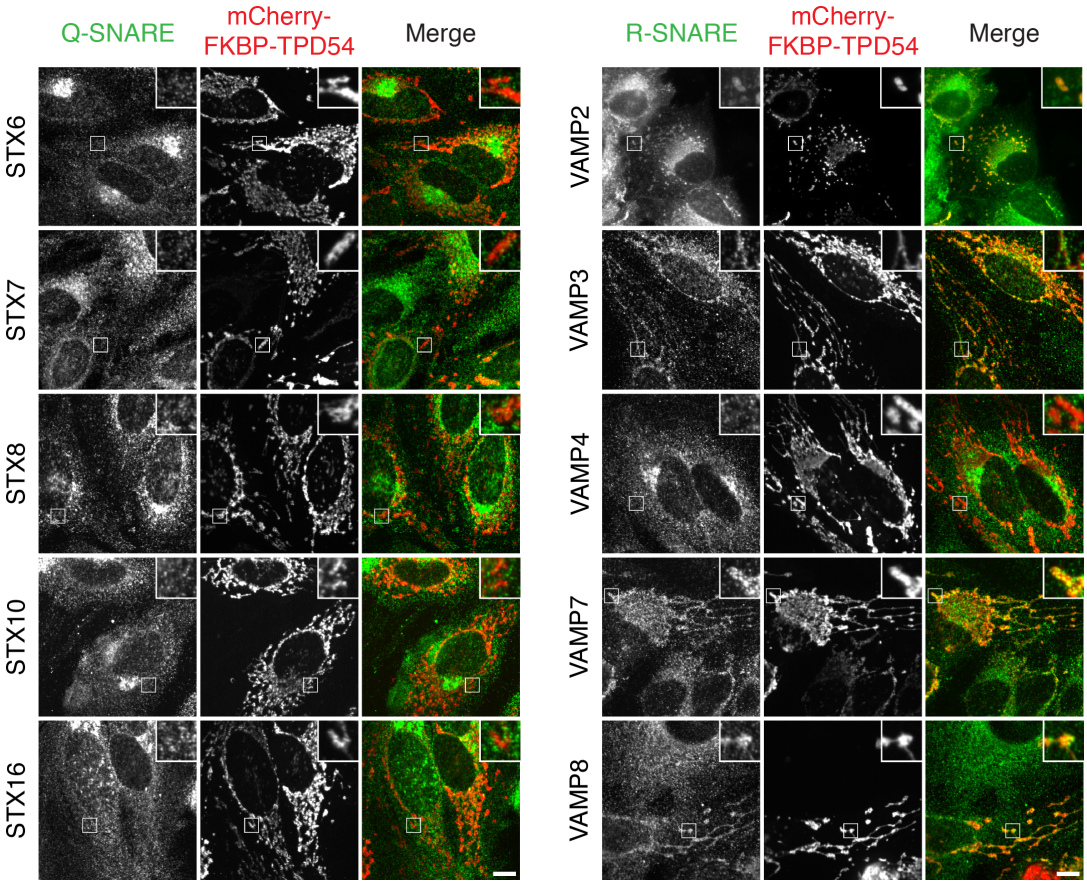

Figure 7. Co-rerouting of R-SNARES but not Q-SNARES, with TPD54.
Representative confocal micrographs showing the co-rerouting of SNAREs as indicated after TPD54 rerouting to mitochondria. SNAREs were detected by immunofluorescence with the exception of VAMP2 which is co-expressed as GFP-VAMP2 (widefield image). Insets, 3× zoom. Scale bar, 10 μm.

presumably bound to other Rabs, that were not rerouted (***Figure 8–Figure Supplement 2***). TPD54 rerouting tended to give a more complete removal of Rab-positive structures from the cytoplasm (***Figure 8–Figure Supplement 1***). This observation supports a promiscuous relationship between various Rabs and TPD54.

Our Rab screen showed that TPD54 is associated with at least 16 different Rab GTPases. What do these Rabs have in common, if anything? We visualized our Rab collection in two different ways. First, we highlighted our positive hits on a cellular map of the trafficking pathways reported to be regulated by these Rab GTPases (***Figure 8–Figure Supplement 3***). Several pathways were "ruled out" due to their governance by Rabs which were negative in our screen. All of our positive hits coincided with anterograde and recycling pathways, which is in agreement with our functional data. However, we noticed that not every Rab on these pathways was a positive hit in our screen, arguing that the association is Rab-dependent rather than pathway-dependent. Second, we marked up our hits on a phylogenetic tree of the Rab collection (***Figure 8–Figure Supplement 4***). This diagram showed that the positive hits generally belonged to a clade, with a common ancestral sequence. This suggested to us that TPD54 binds directly to these particular Rab GTPases rather than being independently localized on the same vesicle. This interpretation is strengthened by co-immunoprecipitation of Rab proteins with GFP-TPD54 in our earlier proteomic study (***Figure 1***B).

TPD54 is a Rab GTPase effector protein

We next tested if TPD54 binds directly to Rab GTPases and if it does so as an effector to the active, GTP-bound form (***Pylypenko et al., 2018***). To do this, we examined binding of recombinant MBP-TPD54-His to GST-Rab1a (positive hit) or GST-Rab6a (negative) in their GDP- or GppNHp-bound form. TPD54 bound to Rab1a, with preferential binding to the GppNHp-form. By contrast, the amount of binding to GST-Rab6a in either form was similar to GST alone (***Figure 9***A-B).

We also performed similar experiments in cells using the co-rerouting approach. Mutants that lock the Rab in an inactive (GDP-bound) or active (GTP-bound) state were made for GFP-tagged Rab30, Rab1a and Rab6a. These constructs were co-expressed with mCherry-FKBP-TPD54 and dark MitoTrap and their co-rerouting to mitochondria after rapamycin addition was compared to their wild-type counterparts (***Figure 9***C). Co-rerouting was seen for the active and wild-type forms of Rab30 and Rab1a, but no change in localization was observed for the inactive mutant of either Rab. No co-rerouting was observed for wild-type, inactive or active mutants of Rab6a. We analyzed the kinetics of TPD54 rerouting and Rab co-rerouting and found no evidence for interaction with the GDP-bound forms (***Figure 9***C). These observations support the idea that TPD54 binds directly to Rabs in their active form, as an effector protein.

Discussion

This study shows that TPD54, an abundant protein in mammalian cells, regulates anterograde membrane traffic and the recycling of endocytosed cargo. We discovered TPD54 is found on numerous small vesicles throughout the cell and that it associates with many Rab GTPases. This promiscuous association of TPD54 with at least one-quarter of the Rabome is likely due to direct binding as an effector to the active, GTP-bound form of the Rab.

We used a knocksideways-based system to detect TPD54 binding partners and the cargoes transported by TPD54-associated vesicles (***Robinson et al., 2010***). There have been previous reports of vesicle capture at mitochondria following knocksideways of gadkin (***Hirst et al., 2015***), or by ectopic mitochondrial expression of Golgins (***Wong and Munro, 2014***). However, the vesicles captured by TPD54 rerouting are smaller, 29.9 ± 9.4 nm in diameter. Few types of vesicles are this small. For example, clathrin-coated vesicles are 50 to 100 nm, COPII-coated vesicles are 60 to 70 nm, and intra-Golgi transport vesicles are 70 to 90 nm (***Vigers et al., 1986***; ***Balch et al., 1994***; ***Orci et al., 2000***). The closest in size are intralumenal vesicles (ILVs) which range from 20 to 100 nm (***Edgar et al., 2014***; ***Raposo and Stoorvogel, 2013***). Besides the mismatch in size profile, the inaccessibility and opposite orientation of ILVs makes them an ill-suited candidate for the vesicles captured by TPD54 rerouting.

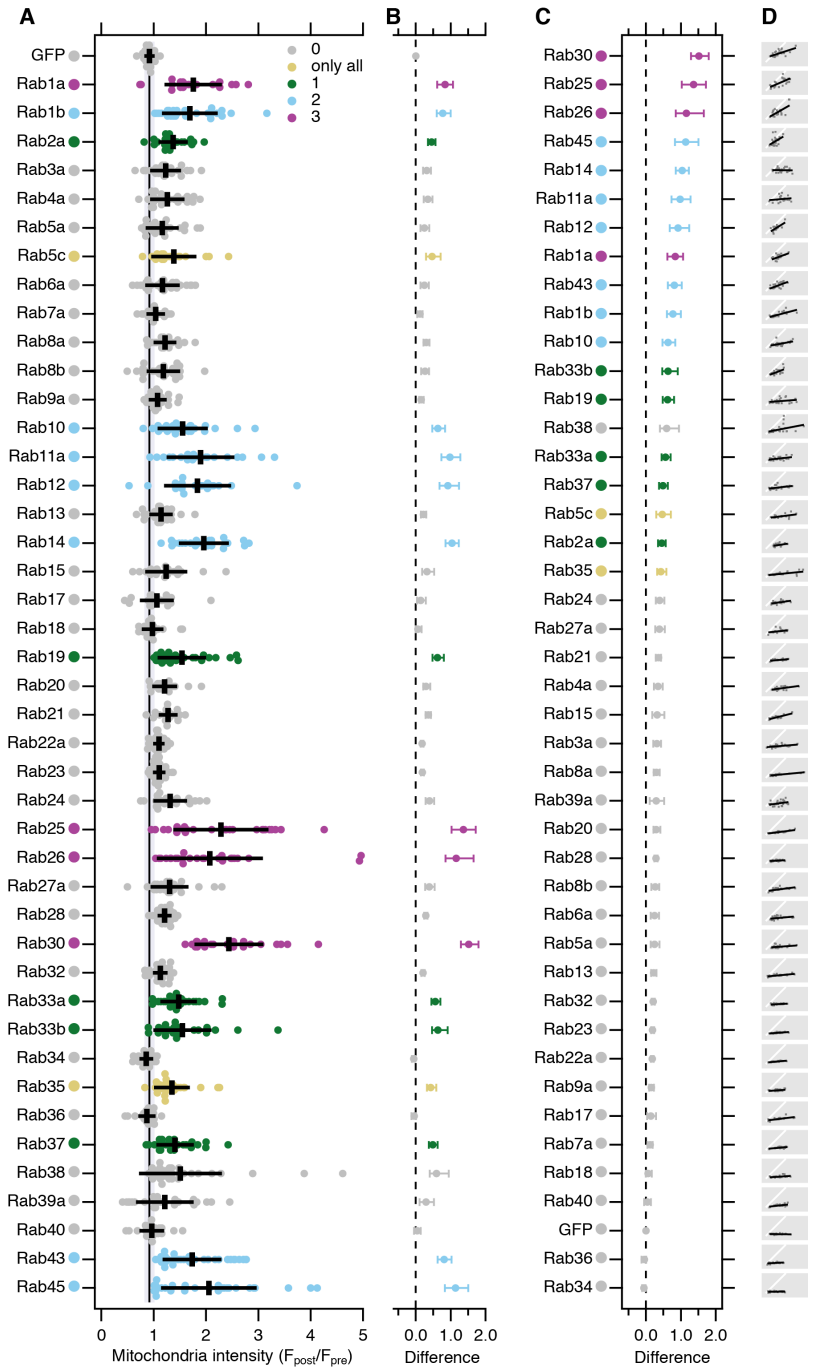

Figure 8. A screen to identify Rab GTPases that are associated with TPD54.
(**A**) Quantification of the change in mitochondrial fluorescence intensity of GFP or GFP-Rabs 2 min after rerouting of mCherry-FKBP-TPD54 to dark MitoTrap with 200 nM rapamycin. Multiple independent experiments were completed (dots) across three independent trials. Black bars, mean ± sd. The mean ± sd for GFP (control) is also shown as a black line and gray zone, down the plot. Dunnett's post-hoc test was done for each trial using GFP as control. Colors indicate if $p < 0.05$ in one, two, three trials or only when all the data were pooled. (**B**) Effect size and bootstrap 95% confidence interval of the data in A. (**C**) The plot in B is ranked from highest to lowest effect size. (**D**) Small multiple plots to show the correlation between the mCherry-FKBP-TPD54 rerouting and GFP-Rabs co-rerouting (gray dots), a line fit to the data (black) and a $y = x$ correlation (white).

Figure 8–video 1. Co-rerouting of GFP-Rab30 (left, green) with mCherry-FKBP-TPD54 (middle, red). Time, mm:ss. Scale bar, 10 μm.

Figure 8–Figure supplement 1. Examples of co-rerouting data from the screen

Figure 8–Figure supplement 2. Reciprocal rerouting of Rabs and TPD54

Figure 8–Figure supplement 3. Cellular localization of the Rabs used in the screen

Figure 8–Figure supplement 4. Phylogenetic tree of the Rab GTPases in the screen

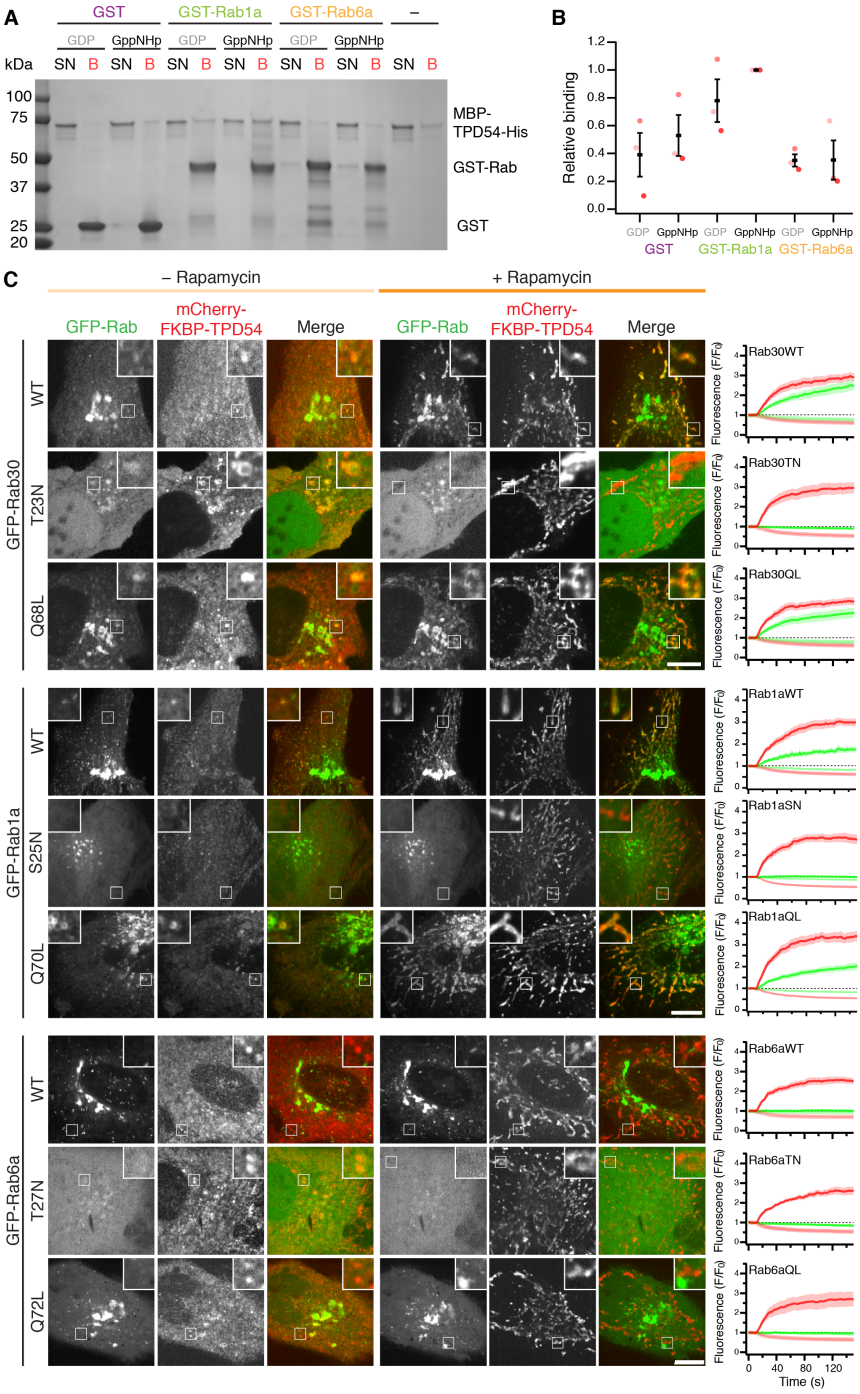

Figure 9. TPD54 binds to active, GTP-bound Rabs.

(**A**) Coomassie-stained SDS-PAGE gel of a GST pull-down assay to test for binding of MBP-TPD54-His to GST, GST-Rab1a or GST-Rab6a in GDP- or GppNHp-loaded states. SN, supernatant; B, beads. (**B**) Quantification of three GST pull-down experiments. MBP-TPD54-His bound to beads, normalized to the GST-Rab1a + GppNHp condition. (**C**) Testing for co-rerouting of the indicated GFP-Rab with mCherry-FKBP-TPD54 to MitoTrap induced by the addition of 200 nM rapamycin. Wild-type Rab30, Rab1a and Rab6a were tested alongside inactive (serine/threonine to asparagine) or active (glutamine to leucine) mutants. Insets, 3× zoom. Scale bars, 10 µm. Rerouting kinetics for TPD54 (red) and Rabs (green) to the mitochondria or from the cytoplasm are shown to the right. Line and shaded region indicate mean ± s.e.m. for the following: Rab30 WT $n = 14$, $\tau_{red} = 31.7$, $\tau_{green} = 38.8$, QL $n = 12$, $\tau_{red} = 25.1$, $\tau_{green} = 45.4$, SN $n = 11$, $\tau_{red} = 25.2$, $\tau_{green} = n.d.$; Rab1a WT $n = 12$, $\tau_{red} = 37.1$, $\tau_{green} = 55.9$, QL $n = 11$, $\tau_{red} = 25.7$, $\tau_{green} = 59.0$, SN $n = 12$, $\tau_{red} = 26.6$, $\tau_{green} = n.d.$; Rab6a WT $n = 12$, $\tau_{red} = 28.0$, QL $n = 10$, $\tau_{red} = 24.0$, SN $n = 6$, $\tau_{red} = 43.1$. Single exponential fits to unweighted averaged data quoted in seconds.

Our interpretation is that the vesicles we have captured are an overlooked class of intracellular vesicle which carry cargo from location A to location B. With no coat to distinguish them and with an unimposing size, these inconspicuous vesicles may have evaded study until now.

The captured vesicles certainly appear to be real, functional transport carriers because they had cargo and fusion machinery. There was selectivity in the cargo, which all contained dileucine-type endocytic motifs and in the R-SNARE complement of the vesicle. The reason for co-rerouting SNAREs could also be due of their dileucine motifs, although we saw no co-rerouting of VAMP4, which has one such motif. The captured vesicles are unlikely to be the result of vesicularization of larger membranes since we saw the capture of 30 nm vesicles after only 20 s of TPD54 rerouting and no further change in size at longer timepoints. Is it possible that TPD54 is on a wider variety of vesicles but that rerouting only captures the smallest of all TPD54-positive vesicles? One could imagine that smaller vesicles are captured more efficiently than larger ones. However, larger vesicles and even Golgi cisternae can be captured by mitochondria under different experimental conditions (***Hirst et al., 2015***; ***Wong and Munro, 2014***; ***Shin et al., 2017***; ***Dunlop et al., 2017***), suggesting that TPD54 is predominantly localized to these small vesicles and that this is the reason for their more efficient capture. This interpretation is supported by live cell imaging and FRAP analyses which suggest that the majority of TPD54 is on the small vesicles.

Using rerouting as a screening method to identify Rabs could be useful for the study of other effector proteins. A previous study used a similar method to demonstrate that the recruitment of Rab5a by its GEF (Rabex-5) depends on GEF activity (***Blümer et al., 2013***). The recruitment was much slower than in our study. There, co-rerouting was on the timescale of several minutes, whereas TPD54 rerouting and co-rerouting of Rabs occurred in seconds. The slow recruitment might be specific to Rabex-5 or to Rab5 and its localization. We identified Rab5c as a TPD54 interactor by proteomics but it was only a borderline hit in our screen. This might mean that co-rerouting of Rab5-vesicles is inefficient. Our screen certainly only reports on Rabs that have the ability to be co-rerouted, a caveat which may mean that we have underestimated the promiscuity of TPD54. An alternative interpretation to explain the difference is that effectors can influence Rab localization more effectively than GEFs.

It is unusual for an effector to bind multiple Rabs. Indeed, the ability of the Rabs to finely tune all parts of the trafficking pathways is in part due to the specificity of their effectors (***Stenmark, 2009***; ***Pylypenko et al., 2018***). There are a few effectors that can bind more than one Rab GTPase. They can do this either by having several Rab binding sites or by virtue of a single site that can bind several Rabs. For example, Rab Coupling Protein (RCP/RAB11FIP1) has one Rab-binding domain through which it can bind Rabs of the same subgroup (Rab11a, Rab 25 and Rab14 in Group IV) (***Lall et al., 2015***; ***Klöpper et al., 2012***). Whereas GCC185, a large, 1684 residue Rab effector, binds Rabs from three different subgroups (I, III and IV), but this occurs via six distinct domains on GCC185 (***Hayes et al., 2009***). To our knowledge, only OCRL1 binds to multiple Rabs (six Rabs from four different subgroups), via a single domain of 123 residues (***Hou et al., 2011***). Our data suggest that TPD54 follows the OCRL1 precedent of being a promiscuous Rab effector, presumably also via a single domain. TPD54 is a small, 206 residue protein and we found association with at least 16 Rab GTPases from three different sub-groups. Effectors generally bind Rabs via one or two helices (***Pylypenko et al., 2018***; ***Rai et al., 2017***). TPD54 has a predicted coiled-coil domain towards the N-terminus, through which it can homodimerize or even heterodimerize with the other TPD52-like proteins (***Byrne et al., 1998***). This could mean that TPD54 as a homodimer binds two Rabs, in a 2:2 configuration described for other effectors such as RCP. These two Rabs would most likely be of the same type as they would be co-resident on the same membrane. One attractive hypothesis is that, by being able to dimerize, TPD54 allows the aggregation of Rabs to create functional sub-domains on vesicles and organelles (***Sönnichsen et al., 2000***; ***Pfeffer, 2010***). Furthermore, its ability to bind many different Rabs could then allow an efficient interplay between Rabs, similar to the one between Rab5 and Rab7 in the maturation of endosomes (***Huotari and Helenius, 2011***). Promiscuity presents a potential problem for Rab regulation if there is cross-talk between different

Rabs. However, the likelihood of crosstalk between say Rab1a on ER-to-Golgi vesicles and Rab25 on recyling vesicles, is remote.

TPD52-like proteins were first identified due to their overexpression in cancer and the expression of TPD52 correlates with a more aggressive metastatic breast cancer phenotype (***Shehata et al., 2008***). Having defined a role for TPD54 in anterograde membrane traffic and cargo recycling through functional studies and by our Rab screen, the next question is if dysregulation of these functions contributes to cancer formation or progression. We note that TPD54 associates with Rab11a and Rab25, two Rabs which are implicated in cancer cell migration and invasion due to their role in integrin recycling (***Caswell et al., 2007***; ***Muller et al., 2009***). Pursuing the role of TPD52-like proteins in membrane traffic in a cancer context is therefore an exciting direction for the future.

Methods

Molecular biology

GFP-TPD54 and mCherry-TPD54 were made by amplifying TPD54 by PCR from human Tumor protein D54 (IMAGE clone: 3446037) and inserted into either pEGFP-C1 or pmCherry-C1 via *Xho*I-*Mfe*I. GFP-TPD52 was made by amplifying TPD52 by PCR from Tumor protein D52 (IMAGE clone: 3916870) and inserted into pEGFP-C1 via *Xho*I-*Mfe*I. GFP-FKBP-TPD54 was made by ligating a *Xho*I-*BamH*I fragment from mCherry-TPD54 into pEGFP-FKBP-C1. This plasmid was converted to mCherry-FKBP-TPD54 by cutting at *BamH*I-*Mfe*I and inserting into pmCherry-C1. MBP-TPD54-His was cloned by inserting TPD54 in pMalPre-His vector via *FseI* and *EagI*.

YFP-MitoTrap and the CD8-chimeras were gifts from Scottie Robinson (University of Cambridge, UK) and mCherry-MitoTrap was previously described (***Cheeseman et al., 2013***). The dark MitoTrap (pMito-dCherry-FRB) has a K70N mutation in mCherry (***Wood et al., 2017***).

The GFP-Rab constructs were a gift from Francis Barr (University of Oxford, UK), except for GFP-Rab1a and GFP-Rab5c. GFP-Rab1a and GFP-Rab5c were made by amplifying human Rab1a or Rab5c (Rab1a: Addgene: #46776, Rab5c: GeneArt synthesis) by PCR and inserting the genes in pEGFP-C1 via *Sac*I-*Kpn*I. Rab mutants GFP-Rab1a S25N and Q70L, GFP-Rab6a T27N and Q66L, and GFP-Rab30 T23N and Q68L were generated from GFP-Rab1a, GFP-Rab6a or GFP-Rab30 using site-directed mutagenesis. GFP-FKBP-Rab11 and GFP-FKBP-Rab25 were a gift from Patrick Caswell (University of Manchester, UK), and GFP-FKBP-Rab7a was made by inserting Rab7a in pEGFP-FKBP-C1 via *Sac*I-*Sal*I. The GST-Rab1a and GST-Rab6a constructs were cloned by cutting Rab1a and Rab6a from GFP-Rab1a and GFP-Rab6a with *Sal*I and *Not*I and inserting into pGEX-6P1.

Plasmid to express mCherry-OCRL1 was a gift from Martin Lowe (University of Manchester, UK). GalT-mCherry was made by cutting GalT via *Bam*HI and *Mfe*I from GalT-CFP (gift from Ben Nichols, MRC Laboratory of Molecular Biology, UK) and inserting into pmCherry-N1. GFP-VAMP2 and mCherry-VAMP2 were made by amplifying VAMP2 from synaptopHluorin (gift from James Rothman, Yale School of Medicine, USA) and inserted into pEGFP-C1 or mRFP-C1 via *Hind*III and *Eco*RI. Other plasmids such as mCherry-LCa were available from previous work (***Hood and Royle, 2009***). SBP-EGFP-E-cadherin and APPL1-mCherry were obtained from Addgene (#65292 and #27683, respectively).

Cell culture

HeLa cells (HPA/ECACC #93021013) were maintained in DMEM supplemented with 10% FBS and 100 U/ml penicillin/streptomycin at 37 °C and 5% CO_2. RNA interference was done by transfecting 100 nM siRNA (TPD54: GUCCUACCUGUUACGCAAU) with Lipofectamine 2000 (Thermo Fisher Scientific) according to the manufacturer's protocol. For DNA plasmids, cells were transfected with a total of 300 ng DNA (per well of a 4-well 3.5 cm dish) using 0.75 µl Genejuice (Merck Millipore) following the manufacturer's protocol. Cells were imaged 1 d after DNA transfection and 2 d after siRNA transfection.

The GFP-TPD54 CRISPR knock-in HeLa cell line was generated by transfecting the Cas9n D10A

nickase plasmid containing the guide pairs (guide 1: 5'ACCGCTGTCGCGGGCGCTAT, guide 2: 5'GCCCGAACATGGACTCCGC) and the repair template. 9 d post-transfection, GFP-positive cells were selected by FACS and isolated. Clones were validated by western blotting and genome sequencing (sequencing primers: 5'CAGTTTCGGCCTATCAGGTTGAGTC, 5'GAACCACACCTCGGAACGGTC, 5'CAGCTTGTGCCCCAGGATGTTG, 5'CAACTACAAGACCCGCGCCGAG).

Biochemistry

For western blot analysis, antibodies used were rabbit anti-TPD54 (Dundee Cell products) 1:1000, mouse anti-α-tubulin (Abcam: ab7291) 1:10000 and mouse anti-GFP clones 7.1 and 13.1 (Sigma Roche: 118144600010) 1:1000.

For the purification of GST, GST-Rab1a and GST-Rab6a, transformed BL21 *Escherichia coli* were grown and proteins induced by addition of 0.5 mM IPTG at 25 °C overnight. Cells were harvested, resuspended in lysis buffer pH8.0 (50 mM Tris, 150 mM NaCl, protease inhibitor tablet (Roche), 0.2 mM PMSF) and lysed by sonication (6× 10 s pulses). The bacterial debris were pelleted at 34 000 g for 30 min at 4 °C. Supernatant was loaded onto a GSTrap FF Columns (GE Healthcare) and washed with high-salt wash buffer pH8.0 (50 mM Tris, 500 mM NaCl, protease inhibitor tablet, 0.1 mM PMSF). Proteins were eluted with elution buffer pH 8.0 (50 mM Tris, 150 mM NaCl, 50 mM glutathione).

MBP-TPD54-His was purified similarly except induction was at 37 °C for 4 h. Cleared supernatant was loaded onto a HisTrap Fast Flow Column (GE Healthcare), proteins were washed with buffer A (20 mM Tris pH8.0, 400 mM NaCl, 0.5 mM $CaCl_2$, 10 mM imidazole) and eluted with buffer B (20 mM Tris pH8.0, 400 mM NaCl, 0.5 mM $CaCl_2$, 400 mM imidazole).

For the Rab binding assay, 3 µM of purified GST, GST-Rab1a or GST-Rab6a was pre-loaded with 300 µM GDP or GppNHp for 90 min at 20 °C in binding buffer (25 mM HEPES, 150 mM KCl, 5 mM $MgCl_2$ pH 7.4). These were incubated with 3 µM of purified MBP-TPD54-His for 90 min at 20 °C. The GST/TPD54 mixture was then incubated with glutathione-sepharose 4B beads for 30 min at 20 °C with rotation and then beads were pelleted. The supernatant was collected and the beads were washed 5× with binding buffer containing 0.1% Tween 20. Proteins were eluted from the beads in Laemmli buffer and boiled. Supernatant and bead fractions were loaded on a 4-15% polyacrylamide gel and visualized by staining with Coomassie brilliant blue.

Immunoprecipitation

Two 10 cm dishes of confluent HeLa cells expressing either GFP or GFP-TPD54 were used for each condition (10 µg DNA transfected per 10 cm dish). Cells were lysed in lysis buffer (10 mM Tris-HCl pH 7.5, 150 mM NaCl, 0.5 mM EDTA, 0.5% NP-40, protease inhibitors (Roche)). The lysate was then incubated for 1 h with GFP-Trap beads (ChromoTek), washed once with exchange buffer (10 mM Tris-HCl pH7.5, 150 mM NaCl, 0.5 mM EDTA) and three times with wash buffer (10 mM Tris-HCl pH7.5, 500 mM NaCl, 0.5 mM EDTA). The immunoprecipitations were run on a 4-15% polyacrylamide gel until they were 1 cm into the gel. The columns were then cut and sent for mass spectrometry analysis to the FingerPrints Proteomics Facility (University of Dundee, UK). Protein scores from four experiments were used to make the volcano plot in `IgorPro`.

Immunofluorescence

HeLa cells grown on cover slips were fixed at room temperature (RT) with 3% paraformaldehyde, 4% sucrose in PBS during 15 min and permeabilized at RT in 0.1% saponin for 10 min (for all staining, unless stated otherwise). For LAMP1 staining, cells were fixed and permeabilized with ice-cold methanol at −20 °C for 10 min. For CD8 staining, cells were fixed in 3% paraformaldehyde, 4% sucrose in PBS during 15 min and permeabilized at RT in 0.5% Triton-X100 in PBS for 10 min. Cells were then blocked in 3% BSA in PBS for 1 h. Cells were incubated for 1 h at RT with primary antibody used as follows: mouse anti-EEA1 (BD Biosciences: 610457) 1 µg/mL, rabbit anti-LAMP1 (Cell Signaling: 9091) 1:200, sheep anti-TGN46 (AbD Serotec: AHP500G) 1.25 µg/mL, mouse anti-CD8 (Biorad:MCA1226GA) 10 µg, rabbit anti-CIMPR (Thermo Fisher: PA3-850) 1:500. Anti-SNARE antibodies were a gift from

Andrew Peden (University of Sheffield, UK). Cells were washed three times with PBS for 5 min and incubated during 1 hour at RT with AlexaFluor (Invitrogen) secondary antibodies. To co-reroute the CD8-EAAALL chimera after timed incubation with anti-CD8 antibodies, cells were labelled with 10 µg AlexaFluor 488- conjugated anti-CD8 antibodies (AbD Serotec, MCA1226A488) at 4 °C for 30 min. Cells were then incubated at 37 °C in warm growth medium for the indicated time points. Rerouting was done by adding 200 nM rapamycin at 37 °C. Cells were fixed and mounted after 5 min, as described above.

For the transferrin assay, HeLa cells grown on coverslips were serum starved for 30 min at 37 °C, then incubated at 4 °C for 30 min with 25 µg/mL of AlexaFluor 488- conjugated transferrin (Thermo Fisher Scientific, 11550756). The coverslips were then dipped in dH_2O, placed in warm growth medium and incubated at 37 °C for 5 to 75 min to allow internalization and recycling, before fixation.

Confocal Microscopy

Cells were grown in 4-well glass-bottom 3.5 cm dishes (Greiner Bio-One) and media exchanged for Leibovitz L-15 CO_2-independent medium for imaging at 37 °C on a spinning disc confocal system (Ultraview Vox; PerkinElmer) with a 100× 1.4 NA oil-immersion objective. Images were captured using an ORCA-R2 digital CCD camera (Hamamatsu) following excitation with 488 nm and 561 nm lasers. For the RUSH assay, SBP-EGFP-E-cadherin was released from the ER by adding a final concentration of 40 µM D-Biotin (Sigma) in L-15 medium. Images were captured at an interval of 2 min. Rerouting of mCherry-FKBP-TPD54 to the mitochondria (dark MitoTrap) was induced by addition of 200 nM rapamycin (Alfa Aesar). Rerouting kinetics experiments were measured by recording movies of 150 s (1 frame per sec), where rapamycin is added after 10 s. The kinetics of mCherry-FKBP-TPD54 rerouting to mitochindria was similar in cells with or without depletion of endogenous TPD54. For the Rab GTPase co-rerouting experiments, an image pre-rapamycin and an image 2 min post-rapamycin was taken of live cells. For the FRAP experiment, a region of 6.69 µm by 10.76 µm was bleached using a 488 nm for five cycles of 100 ms. Images were captured at the highest frame rate possible (0.1775 s).

Correlative light-electron microscopy

Following transfection, cells were plated onto gridded dishes (P35G-1.5-14-CGRD, MatTek Corporation, Ashland, MA, USA). Light microscopy was done using a Nikon Ti epifuorescence microscope, a heated chamber (OKOlab) and CoolSnap MYO camera (Photometrics) using NIS elements AR software. During imaging, cells were kept at 37 °C in Leibovitz L-15 CO_2-independent medium supplemented with 10% FBS. Transfected cells were found and the grid coordinate containing the cell of interest recorded at low magnification. Live cell imaging was done on a cell-by-cell basis at 100x. During imaging, 200 nM (final concentration) rapamycin was added for variable times before the cells were fixed in 3% glutaraldehyde, 0.5% paraformaldehyde in 0.05 M phosphate buffer pH 7.4 for 1 h. Aldehydes were quenched in 50 mM glycine solution and thoroughly washed in H_2O. Cells were post-fixed in 1% osmium tetroxide and 1.5% potassium ferrocyanide for 1 h and then in 1% tannic acid for 45 min to enhance membrane contrast. Cells were rinsed in 1% sodium sulphate then twice in H_2O before being dehydrated in grade series ethanol and embedded in EPON resin (TAAB). The coverslip was removed from the polymerized resin and the grid was used to relocate the cell of interest. The block of resin containing the cell of interest was then trimmed with a glass knife and serial 70 nm ultrathin sections were taken using a diamond knife on an EM UC7 (Leica Microsystems) and collected on formvar coated hexagonal 100 mesh grids (EM resolutions). Sections were post-stained with Reynolds lead citrate for 5 min. Electron micrographs were recorded using a JEOL 1400 TEM operating at 100 kV using iTEM software.

Image analysis

For analysis of RUSH movies, a region of interest (ROI) was drawn around the cell and around the Golgi apparatus in `FIJI`. The area, mean pixel intensity and integrated density was measured

from these ROIs to get fluorescence intensity ratios. Data were processed in IgorPro using custom scripts. Briefly, a logistic function (equation 1) was fitted to the data using the start of the movie and two frames after the maximum value as limits for the fit.

$$f(x) = y_0 + \frac{(y_{max} - y_0)}{1 + (\frac{x_{1/2}}{x})^n} \tag{1}$$

The value for $x_{1/2}$ in minutes was used for the $T_{1/2}$ for ER-to-Golgi. The corresponding y value for $x_{1/2}$ was used to find the $T_{1/2}$ for ER-to-PM. A line of best fit from y_{max} to the end of the trace was found using $f(x) = a + bx$ and the y value corresponding to $y_{x_{1/2}}$ found. The Golgi transit time is taken from the difference between the two $T_{1/2}$ values.

Rerouting kinetics were quantified by averaging the pixel intensity of 10 ROIs of 5x5 pixels on mitochondria and 4 ROIs of varying size in the cytoplasm per cell, in the red, or red and green channels, throughout the duration of the movies. The images were corrected for photobleaching using the simple ratio method prior to measuring pixel intesity for all ROIs. The intensity and time data was fed into IgorPro, and a series of custom-written functions processed the data.

For vesicle capture analysis, electron micrographs were manually segmented in IMOD using a stylus by a scientist blind to the experimental conditions. The coordinates corresponding to contours and objects were fed into IgorPro using the output from model2point. All coordinates were scaled from pixels to real-world values and the vesicle diameters calculated using the average of the polar coordinates around the vesicle center for each vesicle, along with other parameters. As a metric for vesicle capture, the length of the mitochondrial perimeter was measured and used to express the vesicle abundance per image (vesicles per 1 µm). The intersection of an area corresponding to the vesicles, dilated by 15 nm and the mitochondrial perimeter was used to express the fraction of mitochondrial perimeter that was decorated with vesicles.

For the Rab screen, co-rerouting of Rab GTPases was quantified by averaging for each cell, the pixel intensity in the green channel in 10 ROIs of 10x10 pixels on the mitochondria, before and after rapamycin. This mitochondrial intensity ratio (F_{post}/F_{pre}) for every Rab was compared to the ratio of GFP in TPD54-rerouted cells. Estimation statistics were used to generate the difference plot shown in ***Figure 8***B. The mean difference is shown together with bias-corrected and accelerated (BCa) 95% confidence intervals calculated in R using 1×10^5 bootstrap replications.

For FRAP analysis, an ImageJ macro was used to define and measure the GFP intensity (MPD) in the FRAP region, background and whole cell. These data and timestamps from OME were fed into IgorPro for processing. The background-subtracted intensities for the FRAP region and whole cell were used to calculate a ratio (to correct for bleach of molecules induced by the procedure). These values were paired with the timestamps, scaled so that the intensity after bleach was 0 and an average of the first five images minus was 1, and then an interpolated average was created. Fits to individual traces were also calculated using a script. Double exponential function was used for fitting since this gave better fits than a single exponential, particularly for GFP-TPD54, and so that all conditions were fitted in the same way for comparison.

For the Rab binding assay, ROIs of the same area were drawn over the MBP-TPD54-His bands and over the background in the same lanes, and the raw integrated density was measured. The background value was subtracted from the band value and the data was normalized to the MBP-TPD54-His band in the GST-Rab1a (GppNHp) condition.

The phylogenetic tree was generated with phylogeny.fr, using the "one click" mode (***Dereeper et al., 2008***), and was visualized with phylo.io.

All figures were made with either FIJI or Igor Pro 8 (WaveMetrics) and assembled using Adobe Illustrator.

Data and software availability

The data for proteomics, volcano plot, FRAP data and EM segmentation coordinates are available together with code and scripts for analysis https://github.com/quantixed/TPD54/ (***Royle, 2018***).

Acknowledgements

We would like to thank Patrick Caswell, Francis Barr and Andrew Peden for valuable discussion and reagents. We thank Teresa Massam-Wu for purifying MBP-TPD54-His and other members of the lab for constructive criticism and especially, Cecilia Velasco Dominguez, Oliver Sinfield and Andrew Fielding for their earlier work on TPD52 and TPD54. GL was supported by Fonds de recherche du Québec – Nature et technologies and University of Warwick Chancellor's Award. Work in the lab is supported by a Senior Cancer Research UK Fellowship (C25425/A15182) and a Medical Research Council grant (MR/P018947/1).

References

Balch WE, McCaffery JM, Plutner H, Farquhar MG. Vesicular stomatitis virus glycoprotein is sorted and concentrated during export from the endoplasmic reticulum. Cell. 1994 Mar; 76(5):841–852.

Barr F, Lambright DG. Rab GEFs and GAPs. Curr Opin Cell Biol. 2010 Aug; 22(4):461–470. doi: 10.1016/j.ceb.2010.04.007.

Blümer J, Rey J, Dehmelt L, Mazel T, Wu YW, Bastiaens P, Goody RS, Itzen A. RabGEFs are a major determinant for specific Rab membrane targeting. J Cell Biol. 2013 Feb; 200(3):287–300. doi: 10.1083/jcb.201209113.

Boncompain G, Divoux S, Gareil N, de Forges H, Lescure A, Latreche L, Mercanti V, Jollivet F, Raposo G, Perez F. Synchronization of secretory protein traffic in populations of cells. Nat Methods. 2012 Mar; 9(5):493–498. doi: 10.1038/nmeth.1928.

Bucci C, Lütcke A, Steele-Mortimer O, Olkkonen VM, Dupree P, Chiariello M, Bruni CB, Simons K, Zerial M. Co-operative regulation of endocytosis by three Rab5 isoforms. FEBS Lett. 1995 Jun; 366(1):65–71.

Byrne JA, Mattei MG, Basset P. Definition of the tumor protein D52 (TPD52) gene family through cloning of D52 homologues in human (hD53) and mouse (mD52). Genomics. 1996 Aug; 35(3):523–532. doi: 10.1006/geno.1996.0393.

Byrne JA, Nourse CR, Basset P, Gunning P. Identification of homo- and heteromeric interactions between members of the breast carcinoma-associated D52 protein family using the yeast two-hybrid system. Oncogene. 1998 Feb; 16(7):873–881. doi: 10.1038/sj.onc.1201604.

Byrne JA, Tomasetto C, Garnier JM, Rouyer N, Mattei MG, Bellocq JP, Rio MC, Basset P. A screening method to identify genes commonly overexpressed in carcinomas and the identification of a novel complementary DNA sequence. Cancer Res. 1995 Jul; 55(13):2896–2903.

Byrne JA, Maleki S, Hardy JR, Gloss BS, Murali R, Scurry JP, Fanayan S, Emmanuel C, Hacker NF, Sutherland RL, Defazio A, O'Brien PM. MAL2 and tumor protein D52 (TPD52) are frequently overexpressed in ovarian carcinoma, but differentially associated with histological subtype and patient outcome. BMC Cancer. 2010 Sep; 10:497. doi: 10.1186/1471-2407-10-497.

Cao Q, Chen J, Zhu L, Liu Y, Zhou Z, Sha J, Wang S, Li J. A testis-specific and testis developmentally regulated tumor protein D52 (TPD52)-like protein TPD52L3/hD55 interacts with TPD52 family proteins. Biochem Biophys Res Commun. 2006 Jun; 344(3):798–806. doi: 10.1016/j.bbrc.2006.03.208.

Caswell PT, Spence HJ, Parsons M, White DP, Clark K, Cheng KW, Mills GB, Humphries MJ, Messent AJ, Anderson KI, McCaffrey MW, Ozanne BW, Norman JC. Rab25 associates with alpha5beta1 integrin to promote invasive migration in 3D microenvironments. Dev Cell. 2007 Oct; 13(4):496–510. doi: 10.1016/j.devcel.2007.08.012.

Cheeseman LP, Harry EF, McAinsh AD, Prior IA, Royle SJ. Specific removal of TACC3-ch-TOG-clathrin at metaphase deregulates kinetochore fiber tension. J Cell Sci. 2013 May; 126(Pt 9):2102–2113. doi: 10.1242/jcs.124834.

Dasari C, Yaghnam DP, Walther R, Ummanni R. Tumor protein D52 (isoform 3) contributes to prostate cancer cell growth via targeting nuclear factor-κB transactivation in LNCaP cells. Tumour Biol. 2017 May; 39(5):1010428317698382. doi: 10.1177/1010428317698382.

Dereeper A, Guignon V, Blanc G, Audic S, Buffet S, Chevenet F, Dufayard JF, Guindon S, Lefort V, Lescot M, Claverie JM, Gascuel O. Phylogeny.fr: robust phylogenetic analysis for the non-specialist. Nucleic Acids Res. 2008 Jul; 36(Web Server issue):W465–469. doi: 10.1093/nar/gkn180.

Dunlop MH, Ernst AM, Schroeder LK, Toomre DK, Lavieu G, Rothman JE. Land-locked mammalian Golgi reveals cargo transport between stable cisternae. Nat Commun. 2017; 8(1):432. doi: 10.1038/s41467-017-00570-z.

Edgar JR, Eden ER, Futter CE. Hrs- and CD63-dependent competing mechanisms make different sized endosomal intraluminal vesicles. Traffic. 2014 Feb; 15(2):197–211. doi: 10.1111/tra.12139.

Gillingham AK, Sinka R, Torres IL, Lilley KS, Munro S. Toward a comprehensive map of the effectors of rab GTPases. Dev Cell. 2014 Nov; 31(3):358–373. doi: 10.1016/j.devcel.2014.10.007.

Hayes GL, Brown FC, Haas AK, Nottingham RM, Barr FA, Pfeffer SR. Multiple Rab GTPase binding sites in GCC185 suggest a model for vesicle tethering at the trans-Golgi. Mol Biol Cell. 2009 Jan; 20(1):209–217. doi: 10.1091/mbc.e08-07-0740.

Hein MY, Hubner NC, Poser I, Cox J, Nagaraj N, Toyoda Y, Gak IA, Weisswange I, Mansfeld J, Buchholz F, Hyman AA, Mann M. A human interactome in three quantitative dimensions organized by stoichiometries and abundances. Cell. 2015 Oct; 163(3):712–723. doi: 10.1016/j.cell.2015.09.053.

Hirst J, Edgar JR, Borner GHH, Li S, Sahlender DA, Antrobus R, Robinson MS. Contributions of epsinR and gadkin to clathrin-mediated intracellular trafficking. Mol Biol Cell. 2015 Sep; 26(17):3085–3103. doi: 10.1091/mbc.E15-04-0245.

Hood FE, Royle SJ. Functional equivalence of the clathrin heavy chains CHC17 and CHC22 in endocytosis and mitosis. J Cell Sci. 2009; 122(Pt 13):2185–90. https://www.ncbi.nlm.nih.gov/pubmed/19509056, doi: 10.1242/jcs.046177.

Hou X, Hagemann N, Schoebel S, Blankenfeldt W, Goody RS, Erdmann KS, Itzen A. A structural basis for Lowe syndrome caused by mutations in the Rab-binding domain of OCRL1. EMBO J. 2011 Apr; 30(8):1659–1670. doi: 10.1038/emboj.2011.60.

Huotari J, Helenius A. Endosome maturation. EMBO J. 2011 Aug; 30(17):3481–3500. doi: 10.1038/emboj.2011.286.

Johansson M, Rocha N, Zwart W, Jordens I, Janssen L, Kuijl C, Olkkonen VM, Neefjes J. Activation of endosomal dynein motors by stepwise assembly of Rab7-RILP-p150Glued, ORP1L, and the receptor betalll spectrin. J Cell Biol. 2007 Feb; 176(4):459–471. doi: 10.1083/jcb.200606077.

Junutula JR, De Maziére AM, Peden AA, Ervin KE, Advani RJ, van Dijk SM, Klumperman J, Scheller RH. Rab14 is involved in membrane trafficking between the Golgi complex and endosomes. Mol Biol Cell. 2004 May; 15(5):2218–2229. doi: 10.1091/mbc.e03-10-0777.

Kamili A, Roslan N, Frost S, Cantrill LC, Wang D, Della-Franca A, Bright RK, Groblewski GE, Straub BK, Hoy AJ, Chen Y, Byrne JA. TPD52 expression increases neutral lipid storage within cultured cells. J Cell Sci. 2015 Sep; 128(17):3223–3238. doi: 10.1242/jcs.167692.

Kanno E, Ishibashi K, Kobayashi H, Matsui T, Ohbayashi N, Fukuda M. Comprehensive screening for novel rab-binding proteins by GST pull-down assay using 60 different mammalian Rabs. Traffic. 2010 Apr; 11(4):491–507. doi: 10.1111/j.1600-0854.2010.01038.x.

Kitt KN, Hernández-Deviez D, Ballantyne SD, Spiliotis ET, Casanova JE, Wilson JM. Rab14 regulates apical targeting in polarized epithelial cells. Traffic. 2008 Jul; 9(7):1218–1231. doi: 10.1111/j.1600-0854.2008.00752.x.

Klöpper TH, Kienle N, Fasshauer D, Munro S. Untangling the evolution of Rab G proteins: implications of a comprehensive genomic analysis. BMC Biol. 2012 Aug; 10:71. doi: 10.1186/1741-7007-10-71.

Koch D, Rai A, Ali I, Bleimling N, Friese T, Brockmeyer A, Janning P, Goud B, Itzen A, Müller MP, Goody RS. A pull-down procedure for the identification of unknown GEFs for small GTPases. Small GTPases. 2016; 7(2):93–106. doi: 10.1080/21541248.2016.1156803.

Kozik P, Francis RW, Seaman MNJ, Robinson MS. A screen for endocytic motifs. Traffic. 2010 Jun; 11(6):843–855. doi: 10.1111/j.1600-0854.2010.01056.x.

Kulak NA, Pichler G, Paron I, Nagaraj N, Mann M. Minimal, encapsulated proteomic-sample processing applied to copy-number estimation in eukaryotic cells. Nat Methods. 2014 Mar; 11(3):319–324. doi: 10.1038/nmeth.2834.

Lall P, Lindsay AJ, Hanscom S, Kecman T, Taglauer ES, McVeigh UM, Franklin E, McCaffrey MW, Khan AR. Structure-Function Analyses of the Interactions between Rab11 and Rab14 Small GTPases with Their Shared Effector Rab Coupling Protein (RCP). J Biol Chem. 2015 Jul; 290(30):18817–18832. doi: 10.1074/jbc.M114.612366.

Li J, Li Y, Liu H, Liu Y, Cui B. The four-transmembrane protein MAL2 and tumor protein D52 (TPD52) are highly expressed in colorectal cancer and correlated with poor prognosis. PLoS ONE. 2017; 12(5):e0178515. doi: 10.1371/journal.pone.0178515.

Messenger SW, Thomas DDH, Falkowski MA, Byrne JA, Gorelick FS, Groblewski GE. Tumor protein D52 controls trafficking of an apical endolysosomal secretory pathway in pancreatic acinar cells. Am J Physiol Gastrointest Liver Physiol. 2013 Sep; 305(6):G439–452. doi: 10.1152/ajpgi.00143.2013.

Müller MP, Goody RS. Molecular control of Rab activity by GEFs, GAPs and GDI. Small GTPases. 2018; 9(1-2):5–21. doi: 10.1080/21541248.2016.1276999.

Muller PAJ, Caswell PT, Doyle B, Iwanicki MP, Tan EH, Karim S, Lukashchuk N, Gillespie DA, Ludwig RL, Gosselin P, Cromer A, Brugge JS, Sansom OJ, Norman JC, Vousden KH. Mutant p53 drives invasion by promoting integrin recycling. Cell. 2009 Dec; 139(7):1327–1341. doi: 10.1016/j.cell.2009.11.026.

Murray DH, Jahnel M, Lauer J, Avellaneda MJ, Brouilly N, Cezanne A, Morales-Navarrete H, Perini ED, Ferguson C, Lupas AN, Kalaidzidis Y, Parton RG, Grill SW, Zerial M. An endosomal tether undergoes an entropic collapse to bring vesicles together. Nature. 2016; 537(7618):107–111. doi: 10.1038/nature19326.

Nourse CR, Mattei MG, Gunning P, Byrne JA. Cloning of a third member of the D52 gene family indicates alternative coding sequence usage in D52-like transcripts. Biochim Biophys Acta. 1998 Nov; 1443(1-2):155–168.

Orci L, Amherdt M, Ravazzola M, Perrelet A, Rothman JE. Exclusion of golgi residents from transport vesicles budding from Golgi cisternae in intact cells. J Cell Biol. 2000 Sep; 150(6):1263–1270.

Pfeffer SR. How the Golgi works: a cisternal progenitor model. Proc Natl Acad Sci USA. 2010 Nov; 107(46):19614–19618. doi: 10.1073/pnas.1011016107.

Proux-Gillardeaux V, Galli T, Callebaut I, Mikhailik A, Calothy G, Marx M. D53 is a novel endosomal SNARE-binding protein that enhances interaction of syntaxin 1 with the synaptobrevin 2 complex in vitro. Biochem J. 2003 Feb; 370(Pt 1):213–221. doi: 10.1042/BJ20021309.

Pylypenko O, Hammich H, Yu IM, Houdusse A. Rab GTPases and their interacting protein partners: Structural insights into Rab functional diversity. Small GTPases. 2018; 9(1-2):22–48. doi: 10.1080/21541248.2017.1336191.

Pylypenko O, Rak A, Durek T, Kushnir S, Dursina BE, Thomae NH, Constantinescu AT, Brunsveld L, Watzke A, Waldmann H, Goody RS, Alexandrov K. Structure of doubly prenylated Ypt1:GDI complex and the mechanism of GDI-mediated Rab recycling. EMBO J. 2006 Jan; 25(1):13–23. doi: 10.1038/sj.emboj.7600921.

Rai A, Goody RS, Müller MP. Multivalency in Rab effector interactions. Small GTPases. 2017 Jan; p. 1–7. doi: 10.1080/21541248.2016.1265700.

Raposo G, Stoorvogel W. Extracellular vesicles: exosomes, microvesicles, and friends. J Cell Biol. 2013 Feb; 200(4):373–383. doi: 10.1083/jcb.201211138.

Robinson MS, Sahlender DA, Foster SD. Rapid inactivation of proteins by rapamycin-induced rerouting to mitochondria. Dev Cell. 2010 Feb; 18(2):324–331. doi: 10.1016/j.devcel.2009.12.015.

Royle SJ, quantixed/TPD54: First release of TPD54; 2018. https://doi.org/10.5281/zenodo.1585668, doi: 10.5281/zenodo.1585668.

Semerdjieva S, Shortt B, Maxwell E, Singh S, Fonarev P, Hansen J, Schiavo G, Grant BD, Smythe E. Coordinated regulation of AP2 uncoating from clathrin-coated vesicles by rab5 and hRME-6. J Cell Biol. 2008 Nov; 183(3):499–511. doi: 10.1083/jcb.200806016.

Shahheydari H, Frost S, Smith BJ, Groblewski GE, Chen Y, Byrne JA. Identification of PLP2 and RAB5C as novel TPD52 binding partners through yeast two-hybrid screening. Mol Biol Rep. 2014 Jul; 41(7):4565–4572. doi: 10.1007/s11033-014-3327-y.

Shehata M, Bieche I, Boutros R, Weidenhofer J, Fanayan S, Spalding L, Zeps N, Byth K, Bright RK, Lidereau R, Byrne JA. Nonredundant Functions for Tumor Protein D52-Like Proteins Support Specific Targeting of TPD52. Clinical Cancer Research. 2008 Aug; 14(16):5050–5060. http://clincancerres.aacrjournals.org/cgi/doi/10.1158/1078-0432.CCR-07-4994, doi: 10.1158/1078-0432.CCR-07-4994.

Shin JJH, Gillingham AK, Begum F, Chadwick J, Munro S. TBC1D23 is a bridging factor for endosomal vesicle capture by golgins at the trans-Golgi. Nat Cell Biol. 2017 Dec; 19(12):1424–1432. doi: 10.1038/ncb3627.

Sönnichsen B, De Renzis S, Nielsen E, Rietdorf J, Zerial M. Distinct membrane domains on endosomes in the recycling pathway visualized by multicolor imaging of Rab4, Rab5, and Rab11. J Cell Biol. 2000 May; 149(4):901–914.

Stenmark H. Rab GTPases as coordinators of vesicle traffic. Nat Rev Mol Cell Biol. 2009 Aug; 10(8):513–525. doi: 10.1038/nrm2728.

Thomas DDH, Martin CL, Weng N, Byrne JA, Groblewski GE. Tumor protein D52 expression and Ca2+-dependent phosphorylation modulates lysosomal membrane protein trafficking to the plasma membrane. Am J Physiol, Cell Physiol. 2010 Mar; 298(3):C725–739. doi: 10.1152/ajpcell.00455.2009.

Thomas DDH, Weng N, Groblewski GE. Secretagogue-induced translocation of CRHSP-28 within an early apical endosomal compartment in acinar cells. Am J Physiol Gastrointest Liver Physiol. 2004 Jul; 287(1):G253–263. doi: 10.1152/ajpgi.00033.2004.

Tisdale EJ, Bourne JR, Khosravi-Far R, Der CJ, Balch WE. GTP-binding mutants of rab1 and rab2 are potent inhibitors of vesicular transport from the endoplasmic reticulum to the Golgi complex. J Cell Biol. 1992 Nov; 119(4):749–761.

Vigers GP, Crowther RA, Pearse BM. Location of the 100 kd-50 kd accessory proteins in clathrin coats. EMBO J. 1986 Sep; 5(9):2079–2085.

Wandinger-Ness A, Zerial M. Rab proteins and the compartmentalization of the endosomal system. Cold Spring Harb Perspect Biol. 2014 Oct; 6(11):a022616. doi: 10.1101/cshperspect.a022616.

Wilson SH, Bailey AM, Nourse CR, Mattei MG, Byrne JA. Identification of MAL2, a novel member of the mal proteolipid family, though interactions with TPD52-like proteins in the yeast two-hybrid system. Genomics. 2001 Aug; 76(1-3):81–88. doi: 10.1006/geno.2001.6610.

Wong M, Munro S. Membrane trafficking. The specificity of vesicle traffic to the Golgi is encoded in the golgin coiled-coil proteins. Science. 2014 Oct; 346(6209):1256898. doi: 10.1126/science.1256898.

Wood LA, Larocque G, Clarke NI, Sarkar S, Royle SJ. New tools for "hot-wiring" clathrin-mediated endocytosis with temporal and spatial precision. J Cell Biol. 2017; 216(12):4351–4365. doi: 10.1083/jcb.201702188.

Wu YW, Oesterlin LK, Tan KT, Waldmann H, Alexandrov K, Goody RS. Membrane targeting mechanism of Rab GTPases elucidated by semisynthetic protein probes. Nat Chem Biol. 2010 Jul; 6(7):534–540. doi: 10.1038/nchembio.386.

Yoshimura SI, Egerer J, Fuchs E, Haas AK, Barr FA. Functional dissection of Rab GTPases involved in primary cilium formation. J Cell Biol. 2007 Jul; 178(3):363–369. doi: 10.1083/jcb.200703047.

Zhen Y, Stenmark H. Cellular functions of Rab GTPases at a glance. J Cell Sci. 2015 Sep; 128(17):3171–3176. doi: 10.1242/jcs.166074.

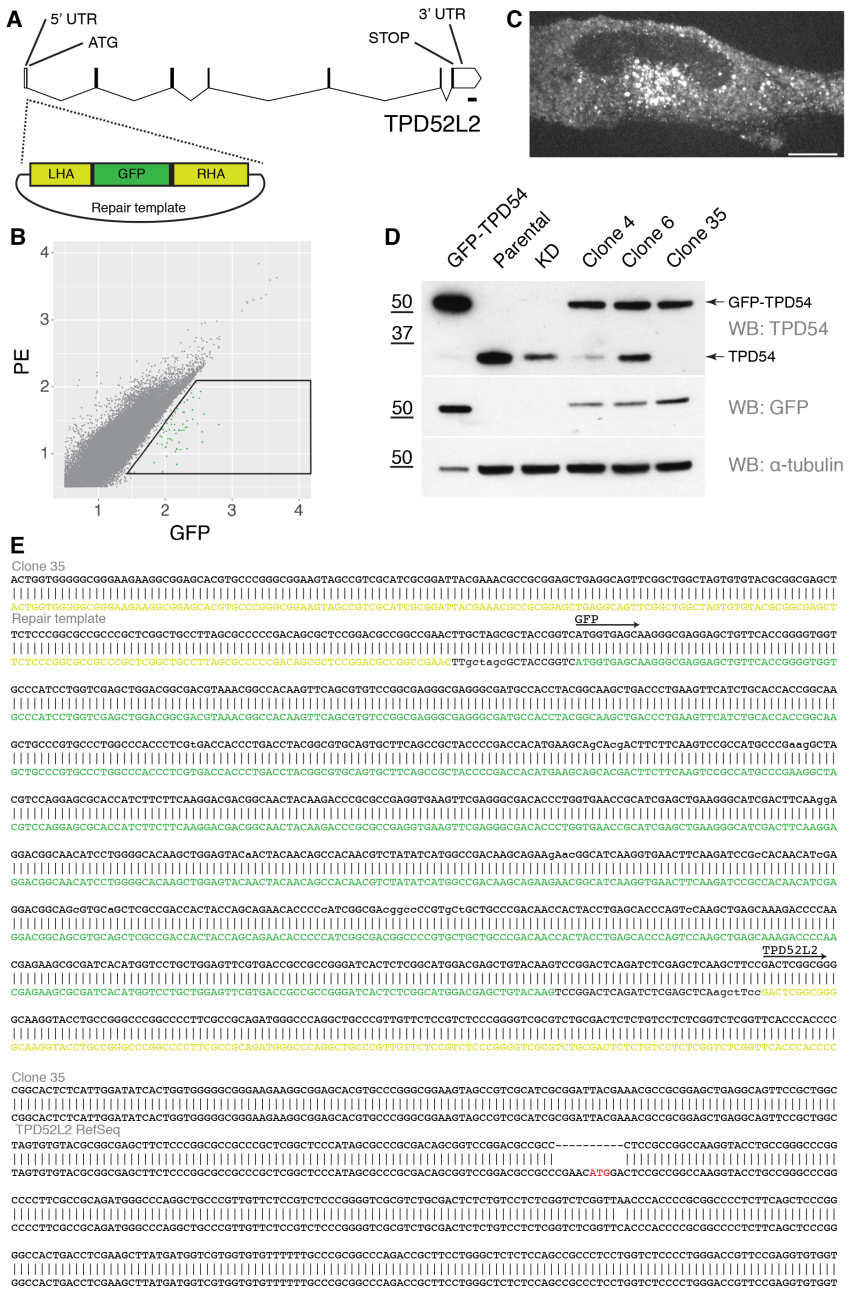

Figure 1–Figure supplement 1. Characterization of the GFP-TPD54 knock-in cell line. (**A**) Gene map of TPD52L2 and location of GFP-tagging. (**B**) FACS plot. GFP-positive cells in the indicated gate were recovered and characterized. (**C**) Representative confocal micrograph of an example GFP-TPD54 knock-in clone. Scale bar, 10 μm. (**D**) Clones were validated by western blot. Cells overexpressing GFP-TPD54, parental HeLa cells, TPD54-depleted cells and three different clones are shown. Clone 35 exhibited the desired band profile. A single GFP-TPD54 band detected by blotting for TPD54 and GFP, with no untagged TPD54. Tubulin is shown as a loading control, note that one-tenth of the GFP-TPD54 transfected sample was loaded. (**E**) Sequencing the TPD52L2 locus in clone 35. Two bands were amplified using primers flanking the integration site. The first sequence shows integration of monomeric GFP between the homology arms, giving GFP-TPD54. The second sequence shows that clone 35 is null at the other allele.

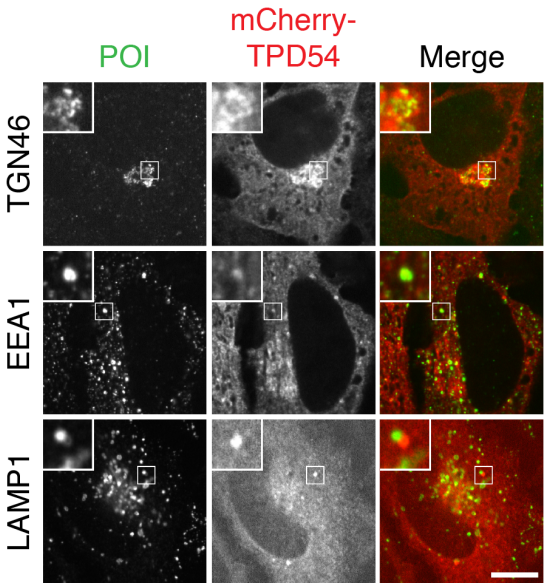

Figure 1–Figure supplement 2. Representative confocal micrographs showing the colocalization of TPD54 with the Golgi apparatus marker TGN46, the early endosomal marker EEA1 and the lysosomal marker LAMP1. Insets: 3X zoom. Scale bar, 10 µm.

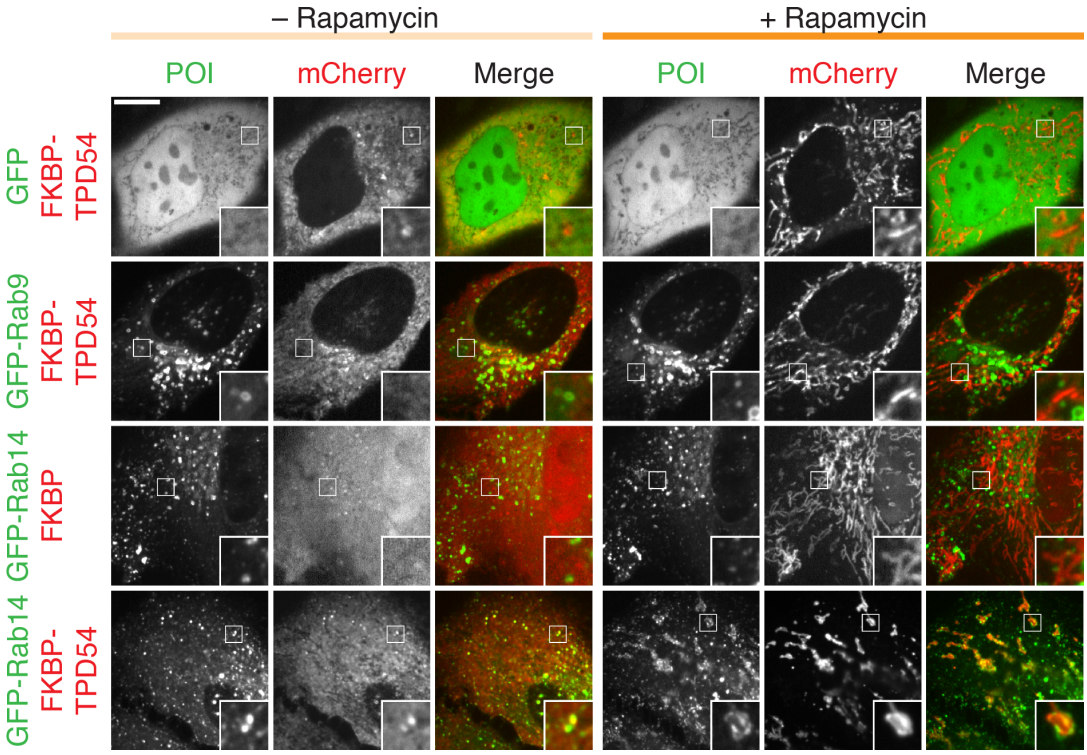

Figure 8–Figure supplement 1. Representative micrographs showing the co-rerouting of GFP-Rab14, but not GFP or GFP-Rab9, after a rerouting of mCherry-FKBP-TPD54 to dark Mitotrap by addition of 200 nM rapamycin. Note that GFP-Rab14 localization is unaffected by rerouting of mCherry-FKBP. Insets, 3× zoom. Scale bar, 10 µm.

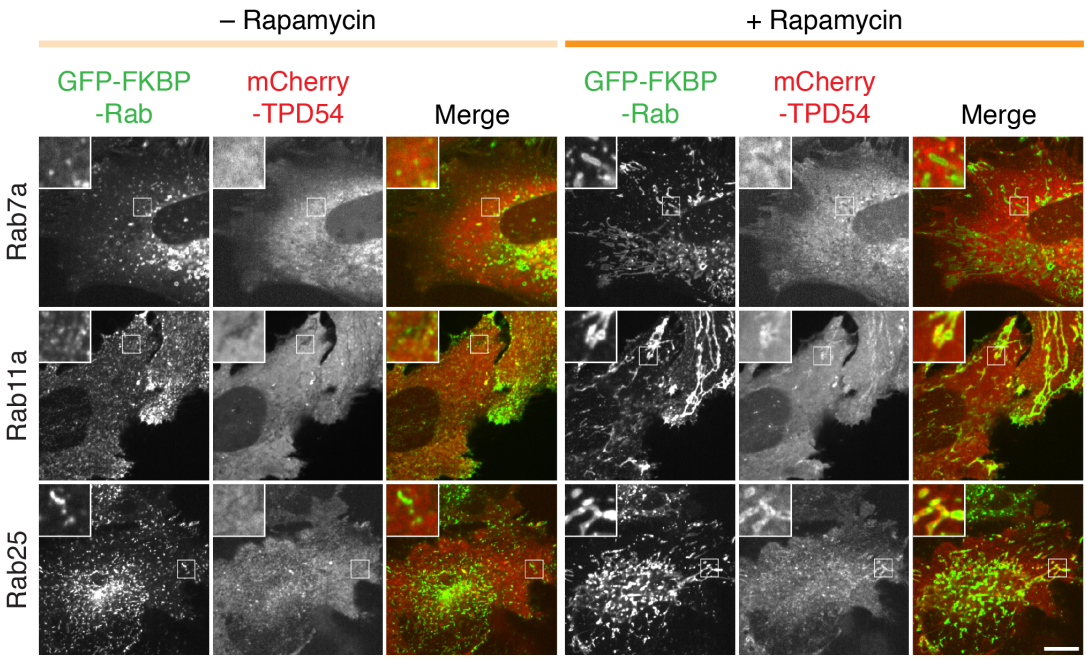

Figure 8–Figure supplement 2. Two positive hits (Rab11a and Rab25) and a negative Rab (Rab7a) were tested for TPD54 co-rerouting. Micrographs of cells before and after rerouting the indicated GFP-FKBP-Rab to dark MitoTrap in cells also expressing mCherry-TPD54. Insets, 3× zoom. Scale bar, 10 µm.

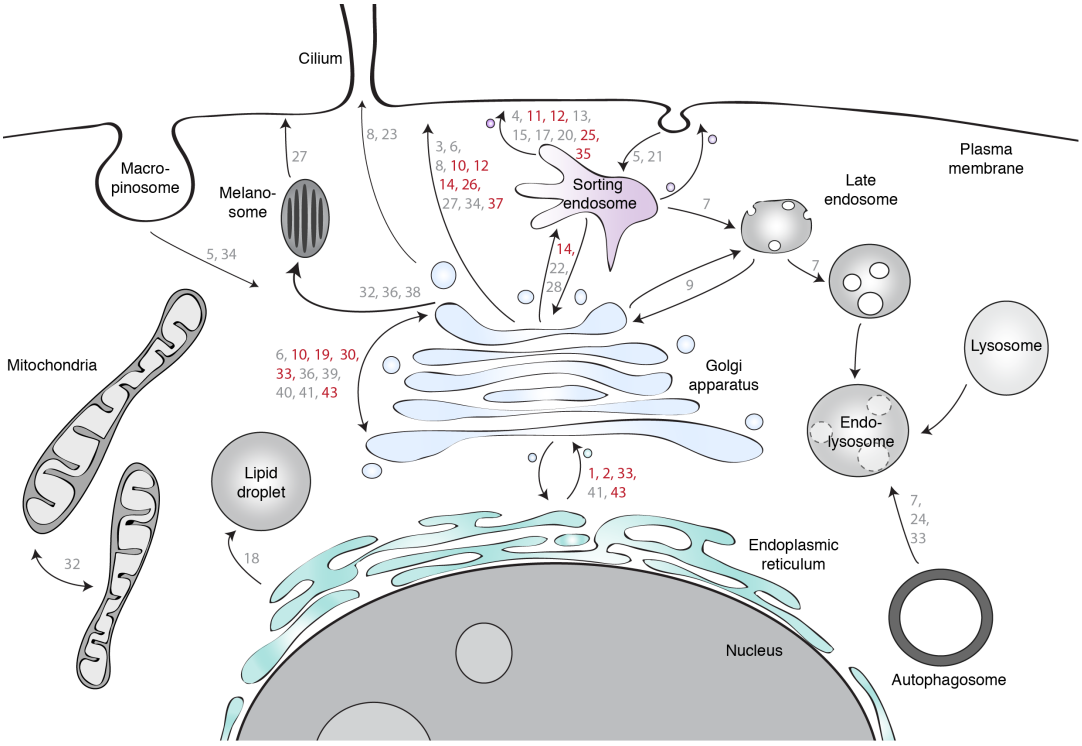

Figure 8–Figure supplement 3. Schematic diagram showing the cellular pathways on which the Rab GTPases operate. Rabs are represented by their number. Red and gray numbers indicate positive and negative Rab hits, respectively.

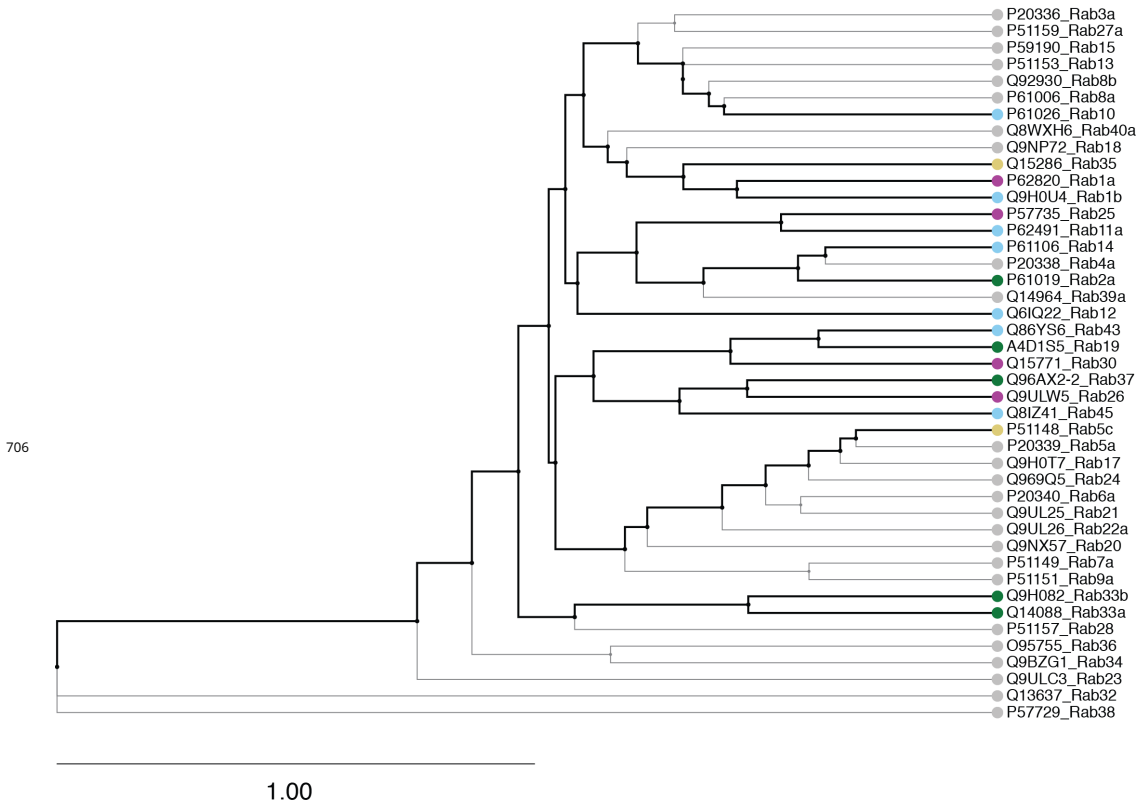

Figure 8–Figure supplement 4. Phylogenetic tree of the Rab GTPases in the screen. Black branches indicate Rabs that interact with TPD54. Colored circles are as described in the main figure.